

One dimensional nexus objects, network of Kibble-Lazarides-Shafi string walls, and their spin dynamic response in polar distorted B-phase of ^3He

K. Zhang^{1,2,*}

¹*Low Temperature Laboratory, Aalto University, P.O. Box 15100, FI-00076 Aalto, Finland*

²*University of Helsinki, Department of Mathematics and Statistics, P.O. Box 68 FI-00014, Helsinki, Finland*

(Dated: June 19, 2022)

The domain wall problem in the axion solution of CP violation in QCD has condensed-matter based analogy in the nafen-distorted superfluid Helium-3. The Kibble-Lazarides-Shafi (KLS) domain wall, which appears during the temperature of early universe cooling down to QCD scale, attaches on the string defects appeared in the first time symmetry break phase transition. Recent experiment in rotating superfluid Helium-3 produced the network of KLS string walls in human controllable system. In this system, the half quantum vortices (HQVs) occur in the first time symmetry break from normal phase vacuum to polar phase, while the KLS domain walls appear and attach on the HQVs in the phase transition from polar phase to polar-distorted B phase. Based on the method of relative homotopy group, the KLS string walls have turned out to be the descendants of HQVs of polar phase. Here we further show the KLS string wall smoothly connects to spin solitons with length scale around ξ_D when the spin orbital coupling is taken into account. This means HQVs are 1D nexus which connects the spin solitons and the KLS domain walls. This is because the subgroup $G = \pi_1(S_S^1, \tilde{R}_2)$ of relative homotopy group describing the spin solitons is isomorphic to the group describing the half spin vortices – the textures of spin degree of freedom of KLS string wall. In the nafen-distorted Helium-3 system, 1D nexus objects and the spin solitons with topological invariant $2/4$ have two different types of network, which are named as pseudo-random lattices of inseparable and separable spin solitons. These two types of pseudo-random lattices correspond to two different representations of G . We discuss the condition under which pseudo-random lattices model works. The equilibrium configuration and surface densities of free energies of pseudo-random lattices are calculated by numeric minimization. Based on the equilibrium spin textures of different pseudo-random lattices, we calculated their transverse spin dynamic response of NMR spectrum, the resulted frequency shifts and $\sqrt{\Omega}$ -scaling of ratio intensity exactly coincide with the experimental measurements. We also discussed the mirror symmetry in the presence of KLS domain wall and the influence of the explicitly break of this discrete symmetry. Our discussions and considerations can be applied to the composite defects in other condensed matter and cosmological system.

I. INTRODUCTIONS

The composite objects formed by topological defects with different dimensions, such as Kibble-Lazarides-Shafi (KLS) string wall^{1,2}, play significant roles in quantum field theory and cosmological models. It typically appears when two different symmetries with well separated energy scales are spontaneously broken.³⁻⁵ Particularly the KLS string wall induces the domain wall problem of the axion solution of the CP violation in QCD.⁵ In the axion solution, two phase transitions successively occur in our universe during its temperature cools down. In the first time transition, the $U(1)_{PQ}$ symmetry of Peccei-Quinn mechanism is spontaneously break, then the axion and string defect appear. When the cosmic temperature reaches the QCD temperate, the $U(1)_{PQ}$ symmetry is explicitly broken by QCD instanton to discrete symmetry and then the domain wall occurs. As a result, the cosmic strings formed in the first time symmetry break become attached on the the domain walls formed under QCD temperature.³ This string wall system is topologically protected and then stable during the evolution of universe. The universe which have this stable structure will be very different with what we have observed. A lots of ideas have been reported to solve this problem, and the corresponding dynamics of decay of the string wall system also be researched.⁶⁻⁹

On the other side, the similar ideas about string wall system are introduced into condensed matter system and soft matter system. These system may provide very stable instances of string wall with human-controllable methods. For example, the ferroelectric nematic liquid crystal was observed recently.¹⁰ The molecules of this liquid crystal has big enough dipole moments and show ferroelectric-like polar arrangement of polarization vectors. The formation of the string wall by two successive phase transitions during cooling down in this new system was expected.¹¹ In this paper, we focus on the nafen-distorted Helium-3 superfluid system.¹² This system generally is belong to nanoconfined superfluid Helium-3. In this kinds of system, the objects with nanometers geometric sizes are immersed in to liquid Helium-3. In the low temperature at which the liquid Helium-3 is superfluid, these objects, which geometric sizes are less than the coherent length of p -wave triplet cooper paring, will strongly modify the microscopic scattering properties of quisiparticle and then induce new stable phases such as stripe phase.¹³⁻¹⁷ The nafen is one of these kinds of nanostructured material which are consist of randomly distributed parallel Al_2O_3 strands with diameter $2 - 3nm$. This

geometric size is far less than the typical coherent length i.e., $20 - 80nm$. The polar phase, which can never be stable in bulk Helium-3, was predicted to be a stable vacuum state in this system¹³ and later be experimentally identified¹⁸. Recently, The Anderson-Fomin theorem, which is the extension of Anderson theorem¹⁹, further explains the reason of the domination of polar phase in this uniaxial system.^{20,21} Moreover, the observation of the T^3 dependence of gap amplitude of polar phase verified the Anderson-Fomin theorem.²² In multi-orbital superconductor, similar extension of the Anderson theorem was also discussed.²³

The observation of stable polar phase provides an ideal platform to research the Alice string i.e., half quantum vortices (HQVs). This cosmic string makes the electric charge of particle changes sign after moving around it.^{24,25} At the 1970s, HQVs were predicted to appear in Helium-3 A-phase^{26,27}. Unfortunately, HQVs have higher energy than phase vortices in A-phase, then it actually never be observed in bulk A-phase. Nevertheless, many researches about the structures, spin dynamics and spin polarization of HQV in A-phase were reported in last few decades years because its unusual properties.²⁸⁻³³ Now this novel string defect can be easily observed in polar phase and PdA phase of nafen-distorted Helium-3 system.^{34,35} The first homotopy group $\pi_1(R_P)$ of polar phase is isomorphic to $\tilde{\mathbb{Z}} = \{n/2 | n \in \mathbb{Z}\}$, where R_P is vacuum manifold of polar phase.³⁷ The coset $\{n'/2 | n' = 2n + 1\}$ of $\pi_1(R_P)$ characterizes the topological stability of HQVs. The appearance of HQVs in polar phase during cooling down from normal phase is an instance of the formation of cosmic strings by symmetry break phase transition in p -wave superfluid system. When the temperature of polar phase superfluid reaches the transition temperature of polar distorted B-phase (PdB), the second symmetry break phase transition occurs.³⁵ In some spatial regions of polar phase which has HQVs generated in the first time transition, the degenerated parameter \hat{d} of spin degree of freedom asymptotically trends to be constant. Thus the vacuum manifold R_2 of PdB, which appears in the second time symmetry break in regions with constant \hat{d} , is smaller than the PdB vacuum manifold R_1 of the whole system. In other word, the inhomogeneous distribution of polar phase degenerate parameter reduces the original vacuum symmetry of normal phase to vacuum symmetry of polar phase in some parts of system.³⁷ This mechanism is quite similar with the explicitly break of the $U(1)_{PQ}$ symmetry by the appearance of QCD instanton in the cosmic domain wall problem.^{8,9} In the vicinity of the second time symmetry break, it is clear that the HQVs formed in polar phase turn to be string-wall composite topological objects described by relative homotopy group $\pi_1(R_1, R_2)$ i.e.,

$$\pi_1(R_P) \cong \pi_1(R_1, R_2), \quad (1)$$

here the disconnected subsets of R_2 form the KLS domain wall as shown in Fig. 1.³⁷

Earlier the non-axial-symmetric core of quantized vortex was suggested by the string-wall system.³⁹⁻⁴² However, the wall between the separated cores is merely around few coherent lengths.⁴³ In contrast, the KLS string wall formed by the two steps phase transition in PdB phase has around 10 to 20 times of dipole lengths, and the length of wall can be controlled by changing the angular velocity of the system. These perfect properties allow the KLS string wall to be experimentally observed in continuous wave NMR experiment.³⁵ The reason which makes PdB phase has these features is the pinning effect of HQVs by nafen strands.^{35,44} The HQVs are strongly pinned and never move once they appear, thus the KLS domain walls formed in the second time symmetry break will not shrink even they have tensions. Another significant consequence of this strongly pinning results from the randomness of distribution of nafen strands. This randomness makes KLS string walls connect to each other randomly and form a random network of composite string-wall system. Because the geometric size of KLS string wall is around dipole length, the spin orbital coupling (SOC) energy further reduces the vacuum manifold of PdB to discrete sets. This gives rise to spin solitons, which are described by relative homotopy group.⁴⁵ Here in this paper, we show the subgroup of the relative homotopy group of spin solitons is isomorphic to the group characterizing the spin degree of freedom of KLS string wall. And then the spin solitons smoothly connect to KLS domain wall via the HQV i.e., HQV is 1D nexus.³⁷ As a result, the network of KLS string walls is also the network of 1D nexus objects, in which randomly distributed spin solitons connect to each others by KLS domain wall. We show under the low angular velocity limit, the random distributed spin soliton network can be mapped to models of regular lattice consist of spin solitons. we named these kinds of models as pseudo-random lattices. We calculate the frequency shifts of spin dynamic response of different pseudo-random lattices under continuous wave drive and the results exactly coincide with the experimental measurements in ref.³⁵

This paper is organized as following sequence. In Sec. II we introduce the gradient energy density and all orientation energy densities in our problem. The healing length ξ_H of magnetic energy and healing length ξ_D of SOC energy are introduced.³⁶ Based on these well separated characteristic lengths we describe the reduced vacuum manifolds of degenerate parameters in different length scales. In Sec. III we utilize the exact sequences of relative homotopy group of the reduced vacuum manifolds to find out the linear topological defects. We find out the group which describes the spin degree of freedom of KLS string wall in the region $\xi_H < r < \xi_D$ and the relative homotopy group of spin solitons when $r > \xi_D$. We prove the former is isomorphic to the subgroup of relative homotopy group of spin solitons, and then the spin soliton are smoothly connected to KLS domain wall via HQV. This means HQV is 1D nexus. Because this subgroup has two different representations, there are two classes of 1D nexus objects. One is connected to inseparable spin solitons and the other is connected to separable spin solitons. In Sec. IV, we discuss the condition under which

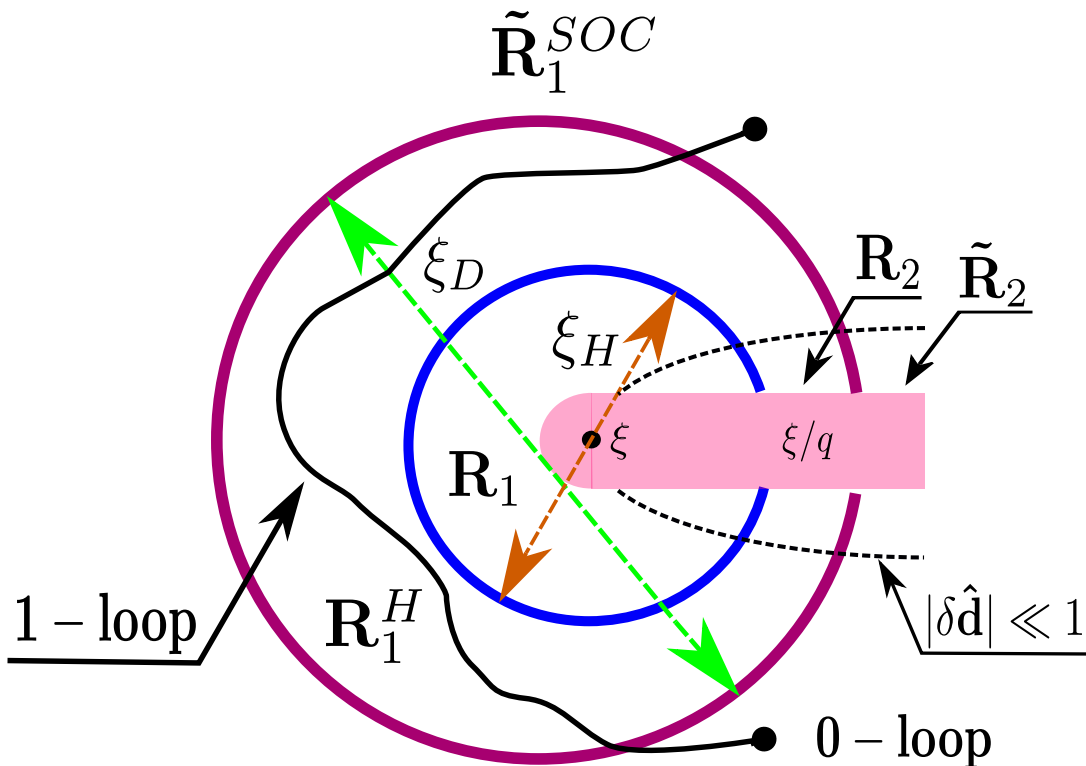


FIG. 1: Illustration of vacua manifolds in length scales $\xi_H < r < \xi_D$ and $r > \xi_D$ in the vicinity of transition from polar phase to PdB phase. As been discussed in Ref.³⁷, the vacua manifolds of PdB in the vicinity of phase transition from polar phase to PdB phase are R_1 and R_2 in the region with $r < \xi_H$. The hierarchy of length scales extends in the presence of magnetic energy and SOC energy. We have known there is KLS string wall described by $\pi_1(R_1, R_2) \cong \hat{\mathbb{Z}}$. In larger region with length scale $\xi_H < r < \xi_D$, R_1 reduces to $R_1^H = S_S^1 \times U(1)^\Phi$ by magnetic energy. To minimize the magnetic energy, spin vectors $\hat{\mathbf{d}}$ perpendicular to static magnetic field $\mathbf{H}^{(0)}$, while the R_2 is unchanged. When taking in account the SOC energy, R_1^H further reduces to $\tilde{R}_1^{SOC} = R_s^{SOC} \times U(1)^\Phi$ and R_2 reduces to $\tilde{R}_2 = \mathbb{Z}_2^{S-\Phi}$. As a results, there are linear topological objects described by $\pi_1(R_1^H, \tilde{R}_1^{SOC})$, in which the relative 1-loop (black solid curve) is mapped to R_1^H while its end points 0-loop is mapped to \tilde{R}_1^{SOC} .

the 1D nexus objects and spin solitons form pseudo-random lattices. The equilibrium configurations of pseudo-random lattices and the corresponding surface densities of free energy are calculated with BFGS optimization. In Sec. V we calculated the spin dynamic response properties of different types of pseudo-random lattices of spin solitons. The results are exactly coincide with the experimental observations. In Sec. VI we discuss the mirror symmetry result from the reduction of vacuum manifold in the presence of KLS domain wall and its explicitly breaking. In Sec. VII we summarize our main results and discuss the possibility of observing the soliton glasses in the presence of coupling between spin solitons under high angular velocity. We also discuss planar spin solitons attached on string monopole networks in PdB phase.

II. VACUUM MANIFOLDS IN THE PRESENT OF MAGNETIC ENERGY AND SPIN-ORBITAL COUPLING ENERGY

The PdB phase achieved by two-step continuous phase transition, which starts from uniaxial anisotropy normal phase vacuum, has two well separated length scales ξ and ξ/q in the vicinity of transition from polar phase to PdB phase.³⁷ In the ref.³⁷, we intensively discussed the vacua manifolds of order parameters of superfluids in the nafen-distorted Helium-3. Those vacua have dramatically different characteristic lengths determined by the energy gaps. As a result, the PdB phase in the vicinity of transition from polar phase to PdB phase has several composite topological objects within different dimensions. Those novel composite objects are classified by relative homotopy groups $\pi_n(R_1, R_2)$ between vacua R_1 and R_2 , where R_1 and R_2 are vacuum manifolds of PdB phase achieved from normal phase vacuum and polar phase vacuum respectively. The stable objects of polar phase are stabilized again in PdB phases by forming composite objects described by relative homotopy groups $\pi_n(R_1, R_2)$.

More length scales appear additionally if we take into account more orientation energies. In nafen-distorted Helium-3 system, those length scales are magnetic length ξ_H and dipole length ξ_D .^{12,36} These two length scales characterize the spatial ranges in which the gradient energy are larger than orientations energies. When the length scale of spatial variations is larger than these characteristic lengths, the vacua manifolds of order parameters are reduced to minimize the orientation energies. We discussed the consequence of this kinds of reduction by magnetic energy and magnetic length ξ_H i.e., the vortex skyrmions in ref.³⁷. We will see there are more interesting results when dipole length ξ_D is introduced in addition to ξ_H in rest parts of the this paper. ξ_H is determined by gradient energy density

$$f_{\text{grad}} = \frac{1}{2}K_1\partial_i A_{\alpha j}\partial_i A_{\alpha j}^* + \frac{1}{2}K_2\partial_j A_{\alpha i}\partial_i A_{\alpha j}^* + \frac{1}{2}K_3\partial_i A_{\alpha i}\partial_j A_{\alpha j}^* \quad (2)$$

where

$$A_{\alpha i} \equiv A_{\alpha i}^{\text{PdB}} = e^{i\Phi}[\Delta_P\hat{d}_\alpha\hat{z}_i + \Delta_{\perp 1}\hat{e}_\alpha^1\hat{x}_i + \Delta_{\perp 2}\hat{e}_\alpha^2\hat{y}_i] \quad (3)$$

is the order parameter of PdB phase. $\hat{\mathbf{d}} \equiv \hat{d}_\alpha$ and $\hat{\mathbf{e}}^{1(2)} \equiv \hat{e}_\alpha^{1(2)}$ are the spin degenerate parameters and they form the triad in spin space. Φ and $\hat{x}_i \equiv \hat{x}_i, \hat{y}_i \equiv \hat{y}_i, \hat{z}_i \equiv \hat{z}_i$ are phase and orbital degenerate parameters respectively. Here $|\Delta_{\perp 1}| = |\Delta_{\perp 2}| = |q|\Delta_P$ with $|q| \leq 1$, and $K_1 = K_2 = K_3$. The magnetic energy density is

$$f_H = -\frac{1}{2}\chi_{\alpha\beta}H_\alpha H_\beta = \frac{1}{2}\gamma_m^2 S_a S_b (\chi^{-1})_{ab} - \gamma_m H_a S_a, \quad (4)$$

here the $\chi_{\alpha\beta}$ is uniaxial tensor of magnetic susceptibility of PdB phase, H_α are magnetic field strengths with $\alpha = 1, 2, 3$, S_a are spin densities with $a = 1, 2, 3$ and γ is gyromagnetic ratio.³⁶ With the help of Eq. (2) and Eq. (4), the magnetic length is given as

$$\xi_H = \left[\frac{K_1 \Delta_P^2}{(\chi_\perp - \chi_\parallel) H^2} \right]^{\frac{1}{2}}, \quad (5)$$

where χ_\perp and χ_\parallel are transverse and longitude spin magnetic susceptibilities of PdB phase. In the experiment for PdB phas, a static magnetic field $\mathbf{H}(0)$ with fixed direction is turned on³⁵. Then the degenerate space of PdB order parameter reduces to

$$R_1^H = S_S^1 \times U(1)^\Phi \quad (6)$$

from R_1 in the region which length scale larger than ξ_H ³⁷. Because the magnetic energy locks the $\hat{\mathbf{d}}$ vector into the plane perpendicular to \mathbf{H} , R_2 keeps the same form as it is inside the region with length scale ξ_H . Then we still have $R_2 = SO_{S-L}(2) \times \mathbb{Z}_2^{S-\Phi}$ in the region where condition $|\delta\hat{\mathbf{d}}| \ll 1$ is satisfied. In Fig. 1, we illustrate the R_1^H and ξ_D in the presence of KLS string wall.

Following the same idea, the dipole length ξ_D is determined by gradient energy density f_{grad} and SOC energy density

$$f_{\text{soc}} = \frac{3}{5}g_D(A_{ii}^*A_{jj} + A_{ij}^*A_{ji} - \frac{2}{3}A_{ij}^*A_{ij}), \quad (7)$$

where g_D is strength of spin orbital coupling. Then we have

$$\xi_D = \frac{5K_1}{6g_D}. \quad (8)$$

When the Spin-Orbit coupling (SOC) is taken into account, degenerate vacuum manifolds of order parameters are further reduced from R_1^H and R_2 . In general consideration, the requirement of minimizing SOC energy in region with length scale larger than ξ_D fixes the relative directions between spin vectors and orbital vectors. The resulted vacuum manifold always could be represented by spin degree of freedom because the broken symmetry is relative symmetry.³⁶ Thus R_1^H reduces to

$$\tilde{R}_1^{\text{SOC}} = R_S^{\text{SOC}} \times U(1)^\Phi \quad (9)$$

in the region with length scale larger than ξ_D , where R_S^{SOC} is the reduced vacuum manifold of spin degree of freedom from R_1^H by SOC. In general case, R_S^{SOC} is a complicated space. However R_S^{SOC} may be simplified by using

parametrization of $\hat{\mathbf{d}}$ and $\hat{\mathbf{e}}^{1(2)}$ vectors of $A_{\alpha i}^{PdB}$. To facilitate comparison between experimental observations and our theoretical analysis, the parametrizations

$$\hat{\mathbf{d}} = \hat{x}\cos\theta - \hat{z}\sin\theta, \quad \hat{\mathbf{e}}^1 = -\hat{x}\sin\theta - \hat{z}\cos\theta, \quad \hat{\mathbf{e}}^2 = \hat{y}, \quad \mathbf{H}^{(0)} = H\hat{y} \quad (10)$$

would be used in this work, where θ is the angle between $\hat{\mathbf{d}}$ and local orbital-coordinate frame.³⁵ In the case, we find $R_S^{SOC} = \{\theta_0, \pi - \theta_0, -\theta_0, \pi + \theta_0\}$, where $\theta_0 = \arcsin[q/(1-|q|)]$. There is a discrete symmetry for free energy of system and this discrete symmetry turns out to be the symmetry between parametrization in Eq. (10) and the alternative one. We will discuss the details of this discrete symmetry and its violation in Sec. VI. Before Sec. VI, we mainly use the parametrization in Eq. (10). In the region in which condition $|\delta\hat{\mathbf{d}}| \ll 1$ is satisfied, This parametrizations fixes the relative rotation of $SO(2)_{S-L}$, thus R_2 reduces to $\tilde{R}_2 = \mathbb{Z}_2^{S-\Phi}$ in the region with length scale larger than ξ_D .

From illustration of R_1^H , \tilde{R}_1^{SOC} and \tilde{R}_2 in Fig. 1, we find again the possibility of utilizing the relative homotopy group to investigate the novel topological objects because of the presence of multiple characteristic length scales.³⁸ This multiple length scales system is belong type (i) of the classifications in Ref.³⁷. Other example of this class is solitons terminated by HQVs observed in spinor Bose condensate with quadratic Zeeman energy.^{46,47} Both of these systems can be described by the first relative homotopy group. In next section, we discuss this topic.

III. SPIN SOLITONS CLASSIFIED BY RELATIVE HOMOTOPY GROUP AND 1D NEXUS OBJECT

A. Relative homotopy groups of spin solitons and 1D nexus objects

1. Spin configuration of HQV – half spin vortices

In the region with length scale $\xi_H \leq r \leq \xi_D$, we have the long exact sequence (LES) of homomorphism of $\pi_1(R_1^H, R_2)$

$$\begin{array}{ccccccc} \pi_1(R_2) & \xrightarrow{i^*} & \pi_1(R_1^H) & \xrightarrow{j^*} & \pi_1(R_1^H, R_2) & \xrightarrow{\partial^*} & \pi_0(R_2) & \xrightarrow{k^*} & \pi_0(R_1^H) \\ \downarrow & & \downarrow & & \downarrow & & \downarrow & & \downarrow \\ \mathbb{Z}^S & \xrightarrow{i^*} & \mathbb{Z}^S \times \mathbb{Z}^\Phi & \xrightarrow{j^*} & \pi_1(R_1^H, R_2) & \xrightarrow{\partial^*} & \mathbb{Z}_2 & \xrightarrow{k^*} & 0 \end{array} \quad (11)$$

where i^* projects spin vortices of $\pi_1(R_2)$ to the spin vortices of $\pi_1(R_1^H)$. And boundary homomorphism ∂^* maps all relative 1-loops of $\pi_1(R_1^H, R_2)$ to their 0-loops of $\pi_0(R_2)$. Because $\pi_0(R_2) = \mathbb{Z}_2$, the end-points of relative 1-loop may take values from connected or disconnected subsets of R_2 . This LES can be spited to the short exact sequence (SES)

$$0 \rightarrow \mathbb{Z}^\Phi \xrightarrow{\iota} \pi_1(R_1^H, R_2) \xrightarrow{\pi} \mathbb{Z}_2 \rightarrow 0, \quad (12)$$

where ι and π are inclusion and surjection respective. Eq. (12) suggests $\pi_1(R_1^H, R_2) \cong \tilde{\mathbb{Z}}$, which is isomorphic to $\pi_1(R_1, R_2)$ in the region smaller than ξ_H ³⁷. This means KLS string wall, which determined by two length scales ξ and ξ/q in two-step phase transition, extends into the region with length scale $\xi_H \leq r \leq \xi_D$. However Eq. (12) only contains degree of freedom (DOF) of phase factor Φ , all information about spin degree of freedom lose because they are trivial element of $\pi_1(R_1^H, R_2)$. To understand the spin part of KLS string wall, we should take in to account the continuity of order parameter. The continuity of order parameter $A_{\alpha i}^{PdB}$ requires spin vectors simultaneously change by $(2n+1)\pi$ in the present of KLS string wall⁴². This consideration suggests that the spin textures are classified by group

$$M \equiv \{n^s/2 | n^s \in \mathbb{Z}\}, \quad (13)$$

which $M/\pi_1(S_S^1) \cong \mathbb{Z}_2 = \{[0], [1/2]\}$. The cosets $[1/2]$ and $[0]$ correspond to the presence or absence of the HQVs in the region $\xi_H < r \leq \xi_D$ respective. Coset $[0] \cong 2\mathbb{Z}$ contains all free spin vortices. While Coset $[1/2] \cong \{n+1/2 | n \in \mathbb{Z}\}$ contains all spin vortices with half-odd winding number i.e., it is set of half spin vortices.

2. Spin soliton described by $\pi_1(R_1^H, \tilde{R}_1^{SOC})$

When taking into account SOC, R_1^H reduces to $\tilde{R}_1^{SOC} = R_S^{SOC} \times U(1)$ as mentioned in Sec. II. As a result, there are linear objects which classified by $\pi_1(R_1^H, \tilde{R}_1^{SOC})$. $\pi_1(R_1^H, \tilde{R}_1^{SOC})$ has long exact sequence (LES)

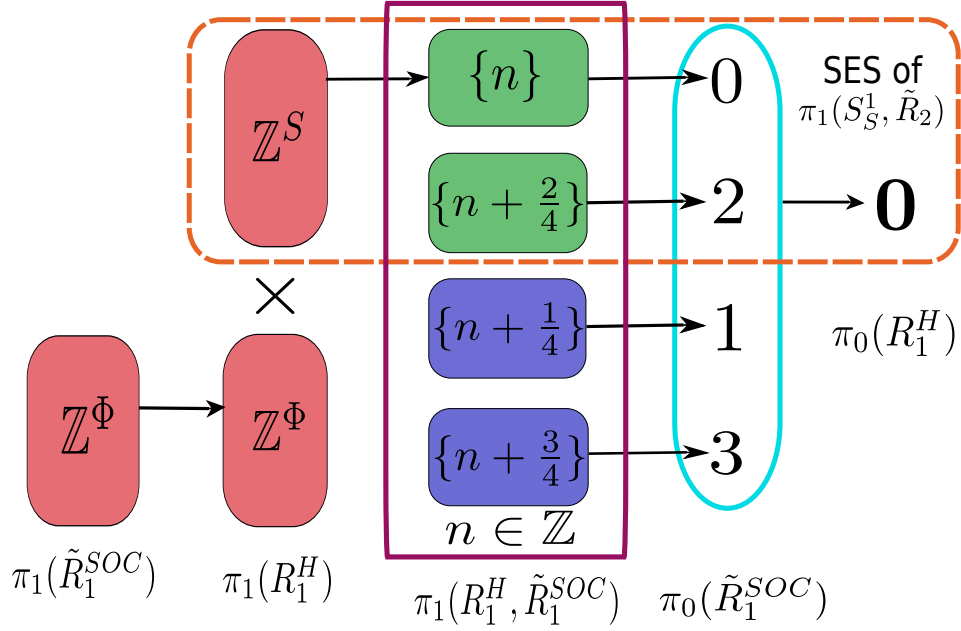


FIG. 2: Illustrations of long exact sequence of homomorphism for $\pi_1(R_1^H, \tilde{R}_1^{SOC})$ and short exact sequence of homomorphism for $\pi_1(S_S^1, \tilde{R}_2)$. The black arrows represent the image of homomorphisms between homotopy groups. This mapping diagram demonstrates the linear objects of $\pi_1(R_1^H, \tilde{R}_1^{SOC})$ are spin solitons. This is because the mapping between $\pi_1(\tilde{R}_1^{SOC})$ and $\pi_1(R_1^H)$ is projection, the image of homomorphism $i^* : \pi_1(\tilde{R}_1^{SOC}) \rightarrow \pi_1(R_1^H) = \mathbb{Z}^\Phi$ i.e., topological invariant of all phase vortices. As a result, the trivial linear objects of $\pi_1(R_1^H, \tilde{R}_1^{SOC})$ are all phase vortices because of $\text{im } i^* \cong \ker j^*$. Moreover, we found there are one kind of spin vortices and three kinds of spin solitons because $\ker k^* \cong \text{im } \partial^* = \mathbb{Z}_4$ and j^* is projection. Moreover, we found from this illustration that the subgroup $G = \{\{n\}, \{n + 2/4\}\}$ of $\pi_1(R_1^H, \tilde{R}_1^{SOC})$ is extension of \mathbb{Z}^S by $\pi_0(\tilde{R}_2^{SOC}) = \mathbb{Z}_2$. In the orange dash line panel, we shows the corresponding short exact sequence of G . As a result, HQVs are 1D nexus between spin soliton of coset $[2/4]$ and KLS domain wall in PdB phase.

$$\begin{array}{ccccccc} \pi_1(\tilde{R}_1^{SOC}) & \xrightarrow{i^*} & \pi_1(R_1^H) & \xrightarrow{j^*} & \pi_1(R_1^H, \tilde{R}_1^{SOC}) & \xrightarrow{\partial^*} & \pi_0(\tilde{R}_1^{SOC}) & \xrightarrow{k^*} & \pi_0(R_1^H) \\ \downarrow & & \downarrow & & \downarrow & & \downarrow & & \downarrow \\ \mathbb{Z}^\Phi & \xrightarrow{i^*} & \mathbb{Z}^S \times \mathbb{Z}^\Phi & \xrightarrow{j^*} & \pi_1(R_1^H, \tilde{R}_1^{SOC}) & \xrightarrow{\partial^*} & \mathbb{Z}_4 & \xrightarrow{k^*} & 0 \end{array} \quad (14)$$

where i^* is projection and ∂^* is boundary homomorphism^{37,38}. Fig. 2 depicts the mapping relation of Eq. (14). The relative 1-loop of $\pi_1(R_1^H, \tilde{R}_1^{SOC})$ and the boundary 0-loop are shown in Fig. 1. Because $\text{im } \partial^* \cong \ker k^* = \mathbb{Z}_4$, the boundary 0-loop (two end points) of 1-loop takes values from four disconnected subsets of \tilde{R}_1^{SOC} . For every element of \tilde{R}_1^{SOC} , there are four possible combinations of elements of \tilde{R}_1^{SOC} for 0-loop. As a result, we found there are four kinds of linear objects in general, which might be distinguished by four boundary homotopy classes of $\pi_0(\tilde{R}_1^{SOC})$. Moreover Eq. (14) can be spited into SES

$$0 \rightarrow \mathbb{Z}^S \xrightarrow{\iota} \pi_1(R_1^H, \tilde{R}_1^{SOC}) \xrightarrow{\partial^*} \mathbb{Z}_4 \rightarrow 0. \quad (15)$$

Then we find $\pi_1(R_1^H, \tilde{R}_1^{SOC}) = \{n^S/4 | n^S \in \mathbb{Z}\} \cong \mathbb{Z}$, with $\pi_1(R_1^H, \tilde{R}_1^{SOC})/\mathbb{Z}^S \cong \mathbb{Z}_4$. Because Eq. (15) is merely determined by $\pi_1(S_S^1) = \mathbb{Z}^S$ and $\pi_0(R_S^{SOC}) = \mathbb{Z}_4$, $\pi_1(R_1^H, \tilde{R}_1^{SOC})$ actually is isomorphic to $\pi_1(S_S^1, R_S^{SOC})$ i.e.,

$$\pi_1(R_1^H, \tilde{R}_1^{SOC}) \cong \pi_1(S_S^1, R_S^{SOC}). \quad (16)$$

This means the linear objects classified by $\pi_1(R_1^H, \tilde{R}_1^{SOC})$ are spin solitons⁴⁵. The four cosets of $\pi_1(S_S^1, R_S^{SOC})$ by \mathbb{Z}^S are

$$[0] = \{n^S\}, [\frac{1}{4}] = \{n^S + \frac{1}{4}\}, [\frac{2}{4}] = \{n^S + \frac{2}{4}\}, [\frac{3}{4}] = \{n^S + \frac{3}{4}\}. \quad (17)$$

The cosets in Eq. (17) give out the topological invariants of the four different kinds of linear objects distinguished by homotopy classes of boundary 0-loop. They correspond to free spin vortices and three kinds of spin solitons

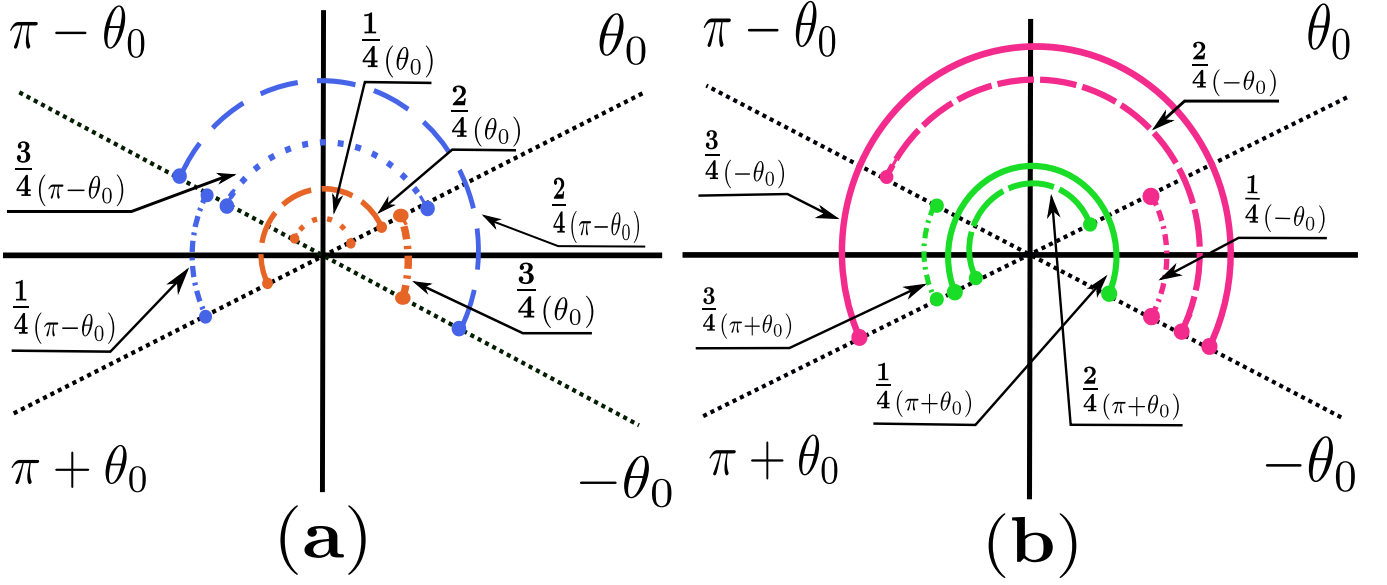


FIG. 3: Illustrations of three kinds of spin solitons described by $\pi_1(S_S^1, R_S^{SOC})$. The black dot lines represent the four elements of R_S^{SOC} i.e., $\pm\theta_0$ and $\pi \pm \theta_0$. The dash line, dot line, dash-dot line and solid line correspond to π -soliton, soliton, KLS-Soliton and big-soliton respective. (a) Spin solitons with topological invariants 1/4, 2/4 and 3/4 for θ_0 (orange) and $\pi - \theta_0$ (blue) respective. (b) Spin solitons with topological invariants 1/4, 2/4 and 3/4 for $-\theta_0$ (pink) and $\pi + \theta_0$ (green) respective.

respectively. Fig. 3 shows the representatives of these three classes of spin solitons for every element of R_S^{SOC} . We omit the spin vortices of [0] from now on because it is not energy-favored stable spin textures. From Fig. 3, we found there are four types of spin solitons distinguished by $|\Delta\theta|$. Following the terminologies in Ref.³⁵, they are big-soliton ($|\Delta\theta| = \pi + 2\theta_0$), soliton ($|\Delta\theta| = \pi - 2\theta_0$), KLS-soliton ($|\Delta\theta| = 2\theta_0$) and π -soliton ($|\Delta\theta| = \pi$). To avoid terminological confusion, we calim here that we use phrase "spin soliton" to denote spin textures of $\pi_1(S_S^1, R_S^{SOC})$ in rest of this paper, while use phrases "solitons", "big-soliton", "KLS-solitons" and " π -solitons" to denote particular spin textures with different $|\Delta\theta|$.

3. Short exact sequence of $\pi_1(S_S^1, \tilde{R}_2)$ and 1D nexus

A significant property of $\pi_1(S_S^1, R_S^{SOC})$ is that it has a subgroup $G \equiv \{[0], [2/4]\}$ such that $G/\mathbb{Z}^S \cong \mathbb{Z}_2$. The SES of G is given as

$$0 \rightarrow \mathbb{Z}^S \rightarrow G \xrightarrow{\partial^*} \mathbb{Z}_2 \rightarrow 0 \quad (18)$$

by Eq. (15). The mapping diagram of Eq. (18) is shown in the dash panel of Fig. 2. Because $\pi_0(\tilde{R}_2) \cong \mathbb{Z}_2$, Eq. (18) can be written as

$$\pi_1(\tilde{R}_2) \rightarrow \pi_1(S_S^1) \rightarrow G \xrightarrow{\partial^*} \pi_0(\tilde{R}_2) \rightarrow 0. \quad (19)$$

This LES suggests

$$G = \pi_1(S_S^1, \tilde{R}_2) \cong \hat{\mathbb{Z}} = M, \quad (20)$$

here $\hat{\mathbb{Z}} \equiv \{n^S/2|n^S \in \mathbb{Z}\}$. Eq. (20) is one of main results of the paper. This relation means spin solitons which are classified by coset $[2/4]$ of $\pi_1(S_S^1, \tilde{R}_2)$ can continuously transform to half spin vortices of M . In other word, KLS domain wall smoothly connects to $[2/4]$ spin soliton via HQV. Similar with 2D nexus which connects string monopoles and vortex skyrmions, the HQV is 1D nexus which connects KLS string wall and $[2/4]$ spin solitons.³⁷ In Sec. III B, we will see there are two possible configurations for $[2/4]$ spin solitons i.e., one π -solitons or a combination between KLS-soliton and soliton.

B. Two different configurations of [2/4] spin soliton – separable and inseparable

Because $\pi_1(S_S^1, R_S^{SOC})/\mathbb{Z}^S \cong \mathbb{Z}_4$, we have $[2/4] = [1/4] + [1/4]$. Thus $\pi_1(S_S^1, \tilde{R}_2)$ could also be represented as $\{[0], [1/4] + [1/4]\}$ besides $\pi_1(S_S^1, \tilde{R}_2) \cong \{[0], [2/4]\}$. This means there are two kinds of spin soliton configurations for a given element of $\pi_1(S_S^1, \tilde{R}_2)$. When the topological invariant is 2/4, the spin soliton is spatially inseparable π -soliton as shown in Fig. 3. When the topological invariant is 1/4 + 1/4, the spin soliton is combination of two spatially separable spin solitons. To identify these two spatially separable spin solitons, we take in account the requirement of continuity of the order parameters. In the London limit, this requirement is equivalent to the requirement of single-value and continuity of θ . Then the accumulation of $|\Delta\theta|$ of those two spin solitons must equal to π . Based on the discussions of Sec. III A 2 and Fig. 3, Those two spin solitons are KLS-soliton and soliton.

We will see these two dramatically different spin texture have different equilibrium free energies, different spin dynamic response properties and different NMR frequency shift in Sec. IV and Sec. V. Those properties help us to distinguish the objects which be observed in experiment.

IV. EQUILIBRIUM TEXTURES OF PSEUDO-RANDOM LATTICES CONSIST OF SPIN SOLITONS

For the PdB phase results from symmetry break of non-uniform polar phase, we can use the Ginzburg-Landau model to describe the system when $|q|$ is small enough. The Ginzburg-Landau free energy consists of gradient energy and orientation energies.³⁶ To quantitatively analyses the equilibrium configurations of spin solitons with length scale around ξ_D , we must find out the extreme point of Ginzburg-Landau free energy under given external parameters. Because $\xi_D \gg \xi_0$ and the strongly uniaxial anisotropy in the presence of nafen strands, we actually did this procedure under London limit.^{36,48,49} In London limit, all gaps parameters attain equilibrium structures and then their magnitudes are constants over whole calculations. When the static magnetic field $\mathbf{H}^{(0)}$ is big enough, the magnetic length ξ_H is far smaller than the dipole length ξ_D , then the magnetic energy has achieved equilibrium everywhere of PdB superfluid. As a result the Ginzbug-Landau free energy in London limit is

$$F_{London} = \int_{\Sigma} (f_{soc} + f_{grad}) d\Sigma, \quad (21)$$

where Σ is the volume of the PdB phase sample.

Plunging $A_{\alpha i}^{PdB}$ into Eq. (21) and substituting $\hat{\mathbf{d}}$, $\hat{\mathbf{e}}^1$ and $\hat{\mathbf{e}}^2$ with their parametrizations in Eq. (10), we get the gradient energy density and SOC energy density in term of θ

$$f_{grad}(\Phi, \theta) = \frac{K_1}{2} (\Delta_P^2 + \Delta_{\perp 1}^2 + \Delta_{\perp 2}^2) \partial_i \Phi \partial_i \Phi + \frac{K_1}{2} (\Delta_P^2 + \Delta_{\perp 1}^2) \partial_i \theta \partial_i \theta + \frac{1}{2} (K_2 + K_3) (\Delta_P^2 \partial_z \Phi \partial_z \Phi \quad (22)$$

$$+ \Delta_{\perp 1}^2 \partial_x \Phi \partial_x \Phi + \Delta_{\perp 2}^2 \partial_y \Phi \partial_y \Phi + \Delta_P^2 \partial_z \theta \partial_z \theta + \Delta_{\perp 1}^2 \partial_x \theta \partial_x \theta), \quad (23)$$

$$f_{soc}(\theta) = \frac{g_D}{5} (\Delta_P^2 + \Delta_{\perp 1}^2 + \Delta_{\perp 2}^2) - \frac{3g_D}{5} (\Delta_P + \Delta_{\perp 1})^2 \cos 2\theta - \frac{6g_D}{5} (\Delta_P + \Delta_{\perp 1}) \Delta_{\perp 2} \sin \theta, \quad (24)$$

where $i = 1, 2, 3$ are the summation indexes of spatial coordinates. In London limit, the term $(g_D/5)(\Delta_P^2 + \Delta_{\perp 1}^2 + \Delta_{\perp 2}^2)$ is a constant over the sample, thus we omit it in the rest of this paper. Because spin degree of freedom dose does not couple with phase degree of freedom, $f_{grad}(\Phi, \theta)$ is simply the summation of $f_{grad}(\Phi)$ and $f_{grad}(\theta)$, where $f_{grad}(\Phi)$ and $f_{grad}(\theta)$ are the gradient energy densities of phase and spin vectors respective. Then we drop $f_{grad}(\Phi)$ in the rest part of this work. Moreover, because the HQVs are pinned by nafen strands, the system is translation invariant along the direction of nafen strands i.e., all $\partial_z \theta$ terms vanishes. Thus the free energy which determines the equilibrium textures of spin solitons is

$$F(\theta)_{London} = \int_{\Sigma} [f_{soc}(\theta) + f_{grad}(\theta)] d\Sigma, \quad (25)$$

where $f_{grad}(\theta)$ and $f_{soc}(\theta)$ are given as

$$f_{grad}(\theta) = \frac{K_1}{2} (\Delta_P^2 + \Delta_{\perp 1}^2) (\partial_x \theta \partial_x \theta + \partial_y \theta \partial_y \theta) + \frac{1}{2} (K_2 + K_3) \Delta_{\perp 1}^2 \partial_x \theta \partial_x \theta, \quad (26)$$

$$f_{soc}(\theta) = -\frac{3g_D}{5} (\Delta_P + \Delta_{\perp 1})^2 \cos 2\theta - \frac{6g_D}{5} (\Delta_P + \Delta_{\perp 1}) \Delta_{\perp 2} \sin \theta. \quad (27)$$

In this section, we utilize the nonlinear optimization BFGS algorithm to minimize the free energy functional Eq. (25).⁵⁰ The saddle points of free energy under different parameters are the equilibrium textures of spin solitons. To facilitate minimization of free energy with nonlinear optimization algorithm, we reduce Eq. (25) to

$$\tilde{F}(\theta)_{London} = \frac{1}{\xi_D} \int_{\Sigma} \left[\frac{1}{2}(\gamma_1 + 2\gamma_2)\partial_x\theta\partial_x\theta + \frac{1}{2}\gamma_1\partial_y\theta\partial_y\theta + \frac{1}{\xi_D^2}(-\frac{1}{2}\cos 2\theta - \gamma_3\sin\theta) \right] d\Sigma \quad (28)$$

by multiplying $(\xi_D K_1 \Delta_P^2)^{-1}$, where

$$q = \frac{\Delta_{\perp 2}}{\Delta_P}, \quad \gamma_1 = 1 + |q|^2, \quad \gamma_2 = |q|^2, \quad \gamma_3 = q(1 + |q|). \quad (29)$$

$(\xi_D K_1 \Delta_P^2)^{-1}$ is also be used as the characteristic unit of London limit free energy in the rest parts of this paper. Before talking about those numerical results and analyzing the corresponding physics, we discuss the random lattice of HQVs and 2/4 spin solitons formed by the random pinning effect of nafen strands.^{35,44} We analyze the condition under which the effects of coupling between spin solitons induced by random distributions of HQVs can be neglected. The random lattice of spin solitons is pseudo-random lattices of spin solitons as long as this condition is satisfied. This allows us to understand the network of 1D nexus objects between 2/4 spin soliton and KLS string wall by calculating and analyzing unit cell of pseudo-random lattices consist of spin solitons.

A. Pseudo-random lattice consist of spin solitons

In the experiment of polar distorted B-phase, the HQVs are pinned by nafen strands when they appear during cooling down. Hence the HQVs and KLS string wall randomly distribute in the PdB sample. The statistic distribution of HQVs is uniform because there is no reason which provides preferable location for HQV. This means the number of HQVs in unit area is constant for rotating PdB superfluid with angular velocity Ω . Then the average area occupied by one HQV is constant as well. We denote the average area occupied by HQV as $A = D(\Omega)^2$, where $D(\Omega)$ is the average distance between two HQVs and $D(\Omega)$ depends on the angular velocity as

$$D(\Omega) = \sqrt{A} = \sqrt{\frac{\kappa_0}{4\Omega}}, \quad (30)$$

where $\kappa_0 = h/2m$ is the circulation quantum of HQV and m is mass of Helium-3 atom^{28,34}. In Fig. 4 (a) and (c), we illustrate the uniformly distributed HQVs with a given Ω . These HQVs, as we have known at Sec. III A and III B, are 1D nexuses which connect 2/4 spin solitons and KLS domain walls. Because the randomly distribution of HQVs, the 2/4 spin solitons are also random distributed over the PdB superfluid. Then the HQVs and spin solitons form a 2D random lattice⁵¹. Those spin solitons have almost identical spin configuration and geometric size determined by gradient energy and SOC energy. Their spin dynamic response under weak magnetic drive are almost identical as well. As a result, The spin dynamic response of those spin solitons under weak drive is independent to the distribution of HQVs and spin solitons. The NMR frequency shift under weak magnetic drive is merely determined by the configuration of one spin soliton, and the total ratio intensity of system is the summation of ratio intensities of all spin solitons. We call this kind of random lattice of HQVs and spin solitons as pseudo-random lattice. This means the spin dynamic response properties of pseudo-random lattice of 2/4 spin solitons are equivalent to the spin dynamic properties of a regular lattice of 2/4 spin solitons. There are two types of regular lattices as shown in Fig. 4 (b) and (d) which correspond to inseparable and separable 2/4 spin solitons respectively.

However, the pseudo-random lattice model is not correct any more when the angular velocity of PdB system increase around a critical value Ω_c . To understand this point, we notice that the average distance $D(\Omega)$ between two HQVs is proportional to $1/\sqrt{\Omega}$ in Eq. (30). This means the configurations between spin solitons will overlap and couple with each other if Ω increases persistently because the characteristic thickness of spin soliton i.e., $\sim 2\xi_D$ is constant under given external parameters. The independence of the spin solitons of HQVs pairs loses when $D(\omega) \sim 2\xi_D$ and the static textures of spin solitons strongly depend on the distribution of HQVs. As a result, the spin dynamic response of the radom lattice of spin solitons under weak magnetic drive also strongly depends on the distribution of HQVs. Thus the upper limit of Ω under which pseudo-random lattice model works is determined by $\sqrt{\kappa_0}/4\Omega_c \sim 2\xi_D$ and then

$$\Omega_c \sim \frac{\kappa_0}{16\xi_D^2}. \quad (31)$$

For PdB system with $\kappa_0 = 6.62 \times 10^{-8} m^2/s$ and $\xi_D \sim 10^{-6} m$ to $\sim 10^{-5} m$, Eq. (31) suggests $\Omega_c \sim 10^1 rad/s$ to $\sim 10^3 rad/s$. Those values is larger enough than the angular velocity of PdB system in the experiment of Ref.³⁵, then pseudo-radom lattice model is good enough and we keep working with it in the rest parts of this paper.

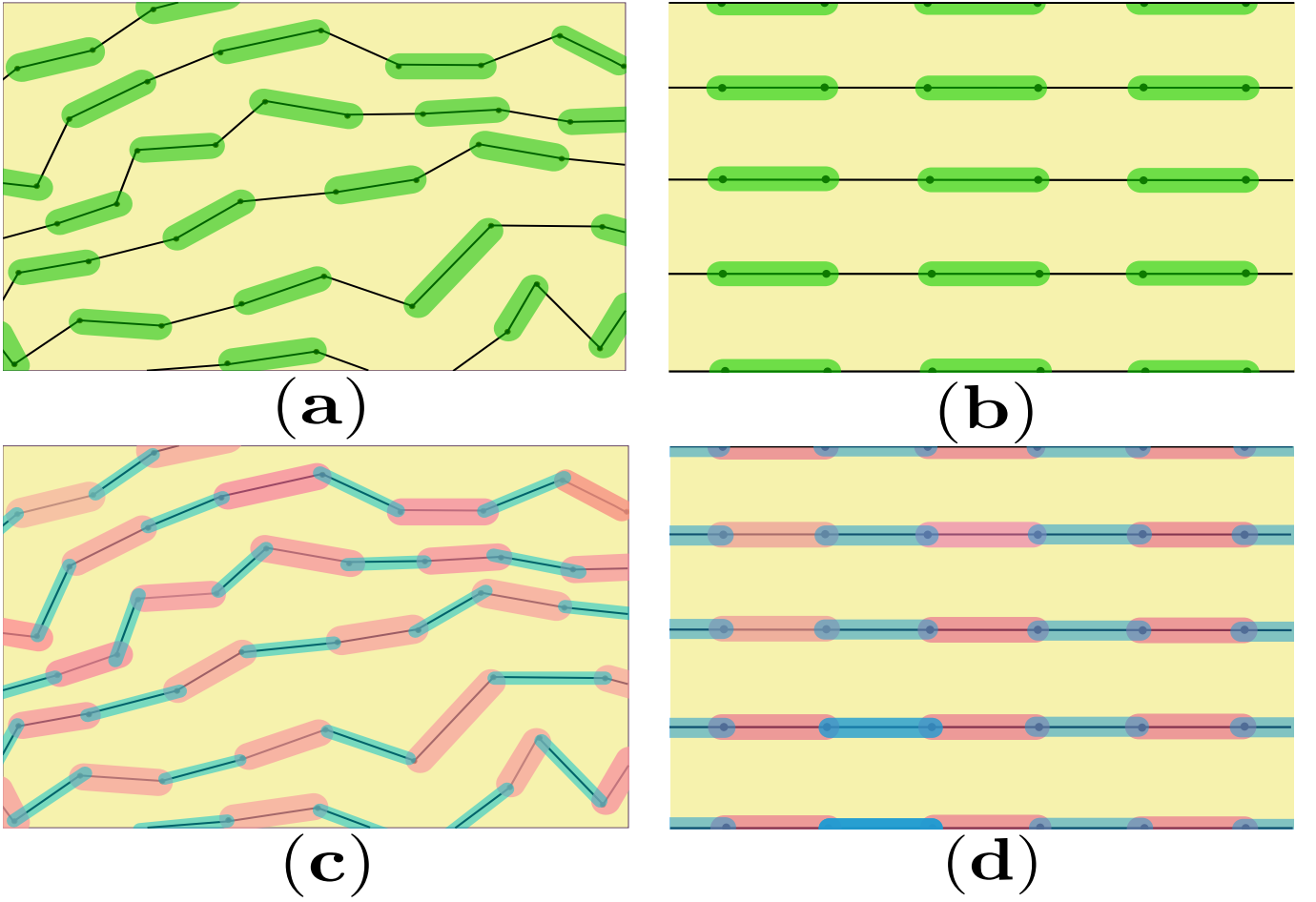


FIG. 4: Illustrations of pseudo-random lattices consist of inseparable and separable spin solitons and their equivalent regular lattices. The black dot represent the HQVs and the black solid lines represent the KLS domain walls. Because every HQV is 1D nexus, two HQVs connect with each others via separable or inseparable 2/4 spin solitons. The small green filled rectangles represent the inseparable spin soliton, while pink and blue filled rectangles represent separable spin solitons. (a) pseudo-random lattice of inseparable spin solitons (π -solitons) at angular velocity $\Omega \ll \Omega_c$. The spin solitons are almost identical and well spatially separated with each others. The spin dynamic response properties of pseudo-random lattice is equivalent to (b) 2D regular lattice of π -solitons. Similarly, (c) pseudo-random lattice of separable spin solitons (KLS-soliton and soliton) has same spin dynamical response with (d) 2D regular lattice consist of KLS-solitons and solitons.

B. Spin solitons in the absence of KLS string wall – Solitons and Big-solitons

To well understand the 1D nexus object consist of 2/4 spin soliton and KLS domain wall, we start from the simpler situation in which it is the absence of KLS string wall. We omit the spin solitons with topological invariant larger than 1 because those kinds of spin solitons cost more energy induced by the existences of spin vortices. In this case $\Delta_{\perp 2}$ is single valued over the sample of superfluid, then only solitons ($|\Delta\theta| = \pi - 2\theta_0$) with topological invariant $1/4_{(\theta_0)}$, $3/4_{(\pi-\theta_0)}$ and big-solitons ($|\Delta\theta| = \pi + 2\theta_0$) with topological invariant $1/4_{(\pi+\theta_0)}$, $3/4_{(-\theta_0)}$ are possible in the system. These two different cases correspond to spin solitons in uniform domain with $\Delta_{\perp 2} = +|q|\Delta_P$ or $\Delta_{\perp 2} = -|q|\Delta_P$ respectively. Moreover, the spin textures have translation symmetry along transverse direction of spin solitons, then the question reduces to one dimensional question in this case. As mentioned before, we use the BFGS non-linear optimization algorithm to minimize the free energy Eq. (28) to get the equilibrium configuration of spin solitons.⁵⁰

In Fig. 5, we show the equilibrium configuration of solitons and big-solitons from $|q| = 0$ to $|q| = 0.2$. The spin textures with $q > 0$ are big-solitons, while the spin textures with $q < 0$ are solitons. We find that the spin vectors of all solitons and big-solitons have common direction $\theta = \pi/2$. This is because $\theta = \pi/2$ is stationary point of $\partial_x \theta$, then $\partial_x \partial_x \theta|_{\theta=\pi/2} = 0$ for all solitons and big-solitons. we will soon see this important feature help us to set appropriate boundary condition for searching equilibrium textures of pseudo-random lattices consist of π -soliton.

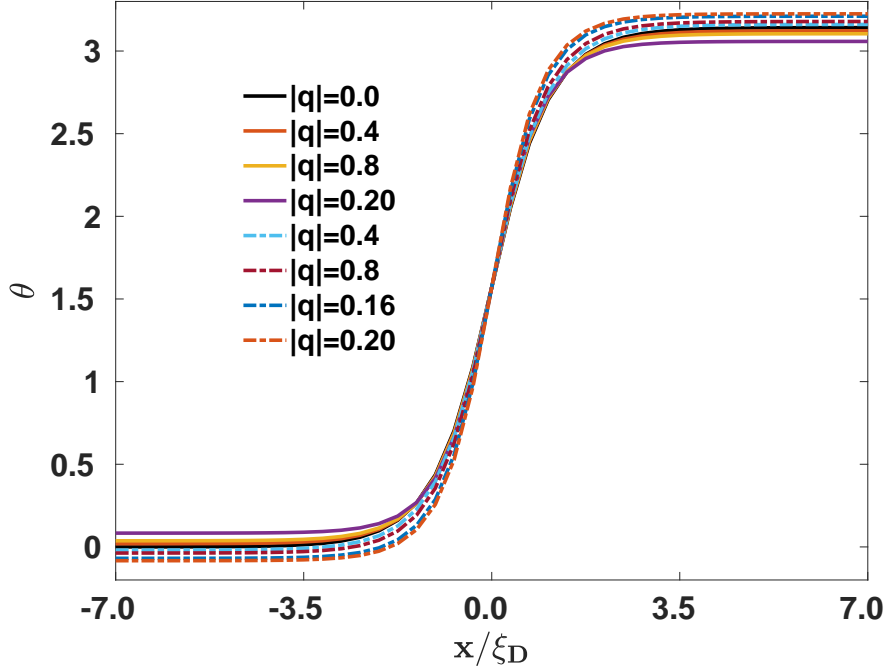


FIG. 5: Equilibrium spin configurations of solitons and big-solitons in uniform domains. Black solid line represents spin soliton of polar phase ($|q| = 0$). The colored dash lines represent big-solitons of PdB phase with $q < 0$ from $|q| = 0.04$ until $|q| = 0.2$. The colored solid lines represent solitons of PdB phase with $q > 0$ from $q = 0.04$ until $q = 0.2$. The spin vectors of all solitons and big-solitons have same relative direction respect to orbital frame because $\theta = \pi/2$ is the stationary point of $\partial_x \theta$.

C. Spin Solitons in the presence of KLS string wall – Inseparable and Separable spin solitons

As we have discussed in Sec. III A 3 and Sec. III B, the HQV is 1D nexus connecting KLS domain wall and $2/4$ spin soliton. The complexity here is the topological invariant $2/4$ has two different representations i.e., literal $2/4$ or $1/4 + 1/4$. Based on the topological analysis, we have known these two cases correspond to inseparable π -soliton configuration and separable configurations consist of KLS-soliton and soliton.

1. Boundary conditions on the KLS domain wall

To quantitatively get the equilibrium spin textures for both configurations of $2/4$ spin soliton, we minimize the London limit free energy Eq. (28) in the presence of KLS domain wall. For parametrization Eq. (10), KLS domain wall separates two domains with opposite $\Delta_{\perp 2}$ in a unit cell of pseudo-random lattice of spin soliton.

However, different with the situation with uniform domain for soliton and big-soliton in section. IV B, the existence of KLS domain wall induces a singularity of the London limit free energy $\tilde{F}(\theta)$. That is because the order parameter $A_{\alpha i}^{PdB}$ in the London limit is ill-defined on the KLS domain wall. As a result, the free energy Eq. (28) and corresponding Lagrangian equation of θ is also ill-defined on the KLS domain wall. On the other hand, we know θ is a continuous function everywhere for $2/4$ spin soliton because the relative 1-loop of $\pi_1(S_S^1, \tilde{R}_2)$ is a continuous mapping. Then θ keeps single-valued and continuous on the KLS domain wall. These facts require us to set a proper boundary condition of θ on the KLS domain wall. The London limit free energy Eq. (28) can be minimized with this boundary condition.

In order to find out this boundary condition properly, we review the fact that the free energy and Lagrangian equation of θ is ill-defined on the KLS domain wall. This means θ of different domains in the vicinity of the KLS domain wall does not relate to each other by Lagrangian equation of θ . Then θ of two different domains separated by KLS domain wall are determined independently in two uniform domains which have opposite $\Delta_{\perp 2}$. In this situation, to keep the continuity of θ on the KLS domain wall, the boundary condition of θ must be a common value for spin

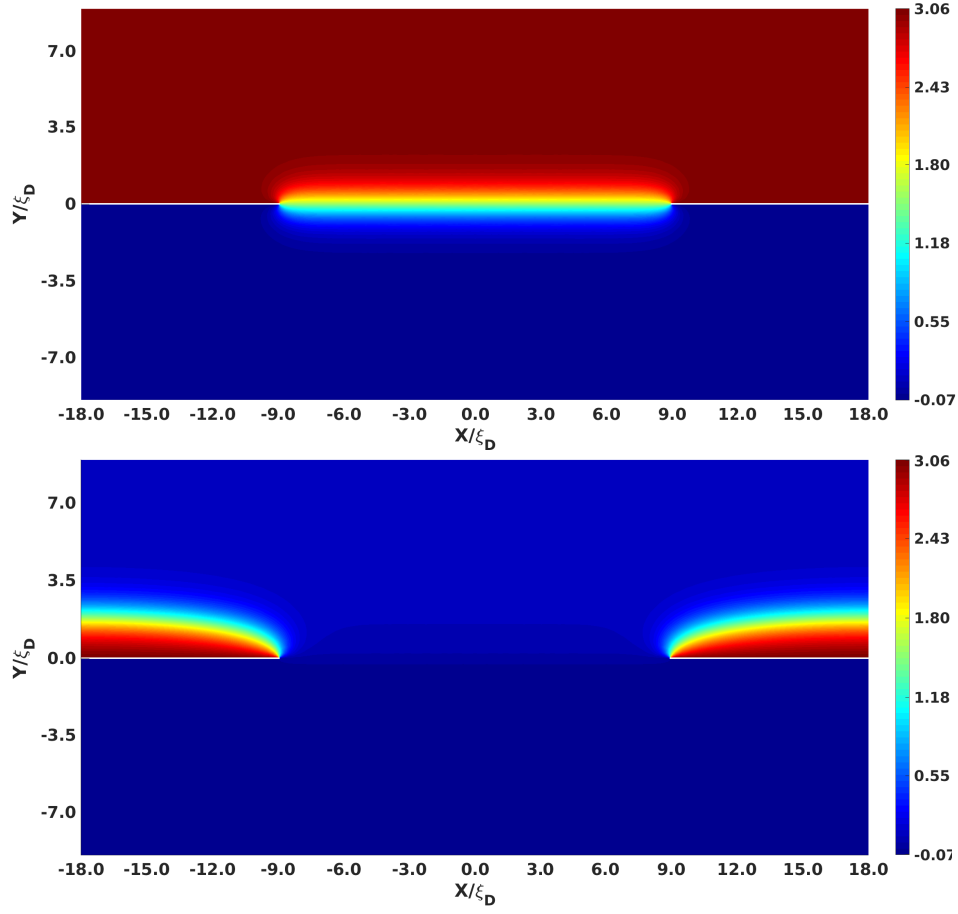


FIG. 6: Equilibrium configurations of unit cell of pseudo-random lattices consist of inseparable spin soliton (π -solitons) and separable spin solitons (KLS soliton and soliton) respectively. These equilibrium spin textures are gotten by minimizing the reduced London limit free energy $\tilde{F}(\theta)_{London}$ in Eq. (28) by BFGS algorithm. The resulted equilibrium distributions of θ depict the equilibrium textures of spin vectors in a unit cell of pseudo-random lattices. (a) depicts the unit cell of inseparable spin soliton (π -soliton) lattice for $|q| = 0.18$ and $D = 18\xi_D$. (b) depicts the unit cell of separable spin soliton (KLS Soliton and soliton) lattice with same parameters but its topological invariant is $1/4 + 1/4$.

solitons in both two domains with opposite $\Delta_{\perp 2}$. For the inseparable spin soliton with topological invariant $2/4$, the natural choice is the stationary point of big-soliton and soliton i.e., $\theta_{KLS} = \pi/2$. This boundary condition indicates the π -soliton may be understood as a hybrid of big-soliton and soliton in London limit. As for the separable spin soliton with topological invariant $1/4 + 1/4$, because all KLS solitons has common values $\theta = 0$ or $\theta = \pi$ on the KLS domain wall, there are two boundary conditions. However, these two boundary conditions are identical, they give rise to same spin textures of pseudo-random lattices consist of separable spin solitons, see details in in appendices Sec. A. Thus in the rest of this paper, we only use $\theta_{KLS} = 0$ for all calculations about separable spin solitons in main text.

2. Equilibrium spin textures and free energies of pseudo-random lattices consist of inseparable and separable $2/4$ spin solitons

In Fig. 6, we show the equilibrium textures of pseudo-random lattices of a pair of separable and inseparable $2/4$ spin solitons with $|q| = 0.18$ and $D = 18\xi_D$. These two equilibrium configurations of a pair of 1D nexus objects are unit cells of pseudo-random lattices of inseparable and separable spin solitons respectively. To collect enough data which could be used to calculate spin dynamic response and compare with experiment, we calculated spin textures with parameters $|q|$ from 0 to 0.2 and D from $4\xi_D$ to $18\xi_D$. Based on these data, we further calculated the reduced London limit free energy Eq. (28) of these two types of pseudo-random lattices of spin solitons lattices, the results are shown in Fig. 7. Before we discussing these numeric results, we firstly evaluate the Eq. (28) for one-half of unit

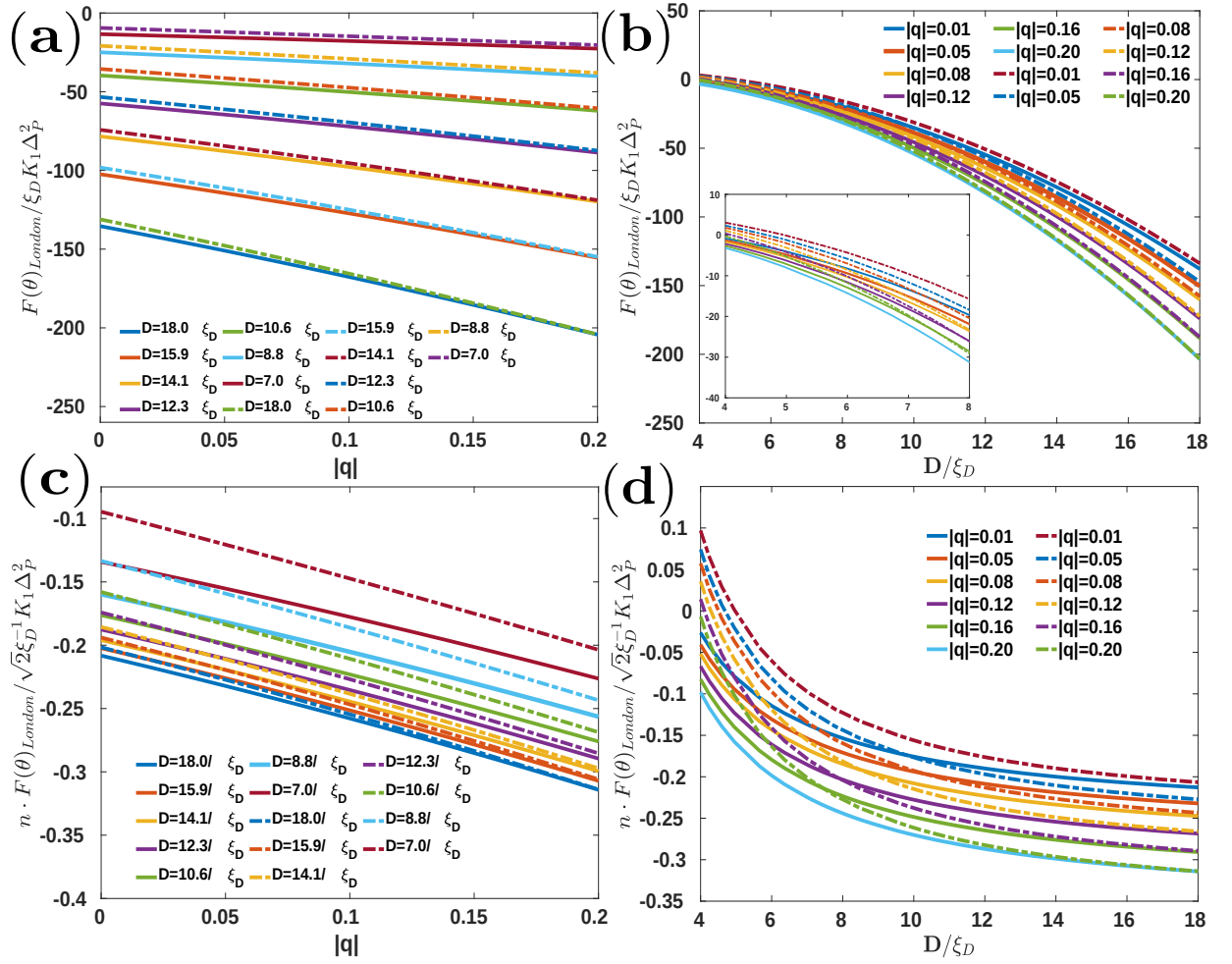


FIG. 7: Free energies $F(\theta)_{London}$ of one-half unit cell and surface densities of free energies $n \cdot F(\theta)_{London}$ of pseudo-random lattices consist of $2/4$ spin soliton with parameters $|q|$ from 0.01 to 0.20 and D from $4\xi_D$ to $18\xi_D$. The reduced free energies $\tilde{F}(\theta)_{London}$ and reduced densities of free energies $n \cdot \tilde{F}(\theta)_{London}$ are calculated based on the equilibrium spin textures of one-half unit cell of the lattices when the pseudo-random lattice model works i.e., $\Omega \ll \Omega_c$. These results depict the equilibrium free energies and energy densities of spin degree of freedom of 1D nexus objects in PdB system. The solid lines represent the inseparable spin solitons, and the dash-dot lines represent the separable spin solitons. (a) shows the free energies $F(\theta)_{London}$ as functions of $|q|$ with different average distances D between HQVs. When SOC energy dominates the system in big enough unit cell, $F(\theta)_{London}$ is monotonically decreasing respect $|q|$. While $F(\theta)_{London}$ does not show remarkably change as $|q|$ changes when gradient energy is competitive to SOC energy in a small enough unit cell. (b) shows the free energies $F(\theta)_{London}$ as monotonically decreasing functions of D . The zooming plot between $4\xi_D$ and $8\xi_D$ in (b) demonstrates this monotonicity is held even when the gradient energy is competitive with the SOC energy in small unit cells. Similarly, (c) depicts the London limit free energy density $n \cdot \tilde{F}(\theta)_{London}$ is monotonically decreasing function of $|q|$. However, (d) demonstrates the London limit free energy densities $n \cdot \tilde{F}(\theta)_{London}$ asymptotically trend to constants determined by SOC energy when SOC energy is the dominating energy in big unit cell. When D is small enough ($D < 6\xi_D$) and gradient energy becomes to the dominating energy, the free energy densities increase rapidly as D decreases because $n \cdot \tilde{F}(\theta)_{London}|_{D < 6\xi_D} \propto 1/D$. All these results show the equilibrium free energies of pseudo-random lattice consist of inseparable spin solitons (π -solitons) are lower than the equilibrium free energies of pseudo-random lattice consist of separable spin solitons (KLS solitons and solitons).

cell when $D \geq 10\xi_D$. In this case,

$$\int_{\Sigma} f_{grad} d\Sigma \sim \frac{1}{2}(1 + |q|^2) \frac{\pi^2 D}{4\xi_D^2} \int_{\Sigma'} d\Sigma, \quad \int_{\Sigma} f_{soc} d\Sigma \sim \int_{\Sigma'} f_{soc} d\Sigma + \int_{\Sigma - \Sigma'} f_{soc} d\Sigma, \quad (32)$$

where Σ' is the region which spin solitons occupy and its area in x - y plane is around $D\xi_D$. Then the integral of f_{soc} in Eq. (32) can be evaluated as

$$\int_{\Sigma'} f_{soc} d\Sigma \sim 0, \quad \int_{\Sigma-\Sigma'} f_{soc} d\Sigma \sim \int_{\Sigma-\Sigma'} f_{soc|y>0} d\Sigma + \int_{\Sigma-\Sigma'} f_{soc|y<0} d\Sigma. \quad (33)$$

The first integral in Eq. (33) vanishes because f_{soc} is not negative-definite function in Σ' . In contrary, f_{soc} has negative-definite equilibrium values in regions $(\Sigma - \Sigma')_{y>0}$ and $(\Sigma - \Sigma')_{y<0}$. Hence

$$\int_{\Sigma-\Sigma'} f_{soc} d\Sigma \sim \frac{5D(D - \xi_D)}{12\xi_D^2 g_D \Delta_P^2} [f_{soc|y>0} + f_{soc|y<0}]_q. \quad (34)$$

As a result, the reduced London limit free energy is evaluated as

$$\tilde{F}(\theta)_{London} \sim \frac{1}{8}(1 + |q|^2) \frac{\pi^2 D}{\xi_D} + \frac{5D(D - \xi_D)}{12\xi_D^2 g_D \Delta_P^2} [f_{soc|y>0} + f_{soc|y<0}]_q. \quad (35)$$

Eq. (35) immediately suggests SOC energy is dominating energy of London limit free energy when the average distance D between 1D nexuses is big enough and the $\tilde{F}(\theta)_{London} < 0$ because $(f_{soc|y>0} + f_{soc|y<0}) < 0$ over $\Sigma - \Sigma'$. For $|q| \in [0, 0.2]$, $\tilde{F}(\theta)_{London}$ in Eq. (35) is around -130 to -200 with $D = 18\xi_D$. This is exactly what the numeric results show in Fig. 7(b). When D decreases during the angular velocity Ω of PdB system increases, Eq. (35) increases monotonically as shown in Fig. (7) (a) and (b). Other information which Eq. (35) indicates is the London limit free energy of unit cell of pseudo-random lattice is decreasing function for $|q|$ as long as SOC energy is dominating energy. This is because $f_{soc|y>0} + f_{soc|y<0}$ is decreasing function of $|q|$. However, this is not true any more when D is small enough. Because SOC energy is not dominating energy in this case, the positive-definite gradient energy is competitive with SOC energy. As a result, we can find from Fig. (7) (a) and (b) that the $\tilde{F}(\theta)_{London}$ of one-half unit cell does not have remarkably change for different $|q|$ in a small unit cell around $D \sim [4\xi_D, 8\xi_D]$. The free energy density of per unit area of equilibrium pseudo-random lattices can be evaluated by multiplying the surface density of 1D nexuses $n = D^{-2}$ to the Eq. (35),

$$n \cdot \tilde{F}(\theta)_{London} \sim \frac{1}{8}(1 + |q|^2) \frac{\pi^2}{\xi_D D} + \frac{5}{12\xi_D^2 g_D \Delta_P^2} [f_{soc|y>0} + f_{soc|y<0}]_q. \quad (36)$$

Then we found the London limit free energy density of pseudo-random lattices trend to be a constant determined by q when SOC energy is the dominating energy. We can clearly see this from Fig. 7(d) when D is larger than $10\xi_D$. From Eq. (36), we find $n \cdot \tilde{F}_{London}$ is around $10^{-1} \sqrt{2} \xi_D^{-1} K_1 \Delta_P^2$ for $|q| \in [0, 0.2]$ when $D > 10\xi_D$. This coincides with the numerical results in Fig. 7 (c) and (d). When the system is dominated by gradient energy if D is small enough, the free energy density increase rapidly as shown in Fig. (7) (d). If the angular velocity increase successively, the system will go into a parameters region in which pseudo-random model violates.

In all cases, we found the equilibrium free energies of one-half unit cell of separable spin solitons (KLS solitons and solitons) are slightly higher than those of inseparable spin solitons (π -solitons). As a result, the equilibrium free energy densities of pseudo-random lattices consist of separable spin solitons (KLS solitons and solitons) are also slightly higher than those of inseparable spin solitons (π -solitons). This significant fact suggests that the equilibrium states which was observed in experiment of rotating PdB system is the pseudo-random lattice of inseparable $2/4$ spin solitons (π -solitons). We will see this is true in next section by calculating the spin dynamic response of system under weak magnetic drive.

V. SPIN DYNAMIC RESPONSE AND NMR OF PSEUDO-RANDOM LATTICES CONSIST OF $2/4$ SPIN SOLITONS

We have talked the topological origin of 1D nexus objects as well as the inseparable and separable spin solitons with topological invariant $2/4$ in previous sections. These two kinds of spin solitons connecting with KLS string wall have different equilibrium free energies. Thus the pseudo-random lattices consist of them have different equilibrium free energy densities. To compare with the experiments and check the theories, we must calculate the spin dynamic response of system under continuous wave magnetic drive. Under weak enough magnetic drive, the nuclear spin magnetizations of PdB superfluid response a nuclear magnetic resonance (NMR) when the frequency of weak magnetic drive matches the transverse spin dynamic mode. Because the spin dynamics of symmetry broken states of Helium-3 is strongly influenced by SOC energy which is determined by the relative orientations of degenerate parameters of

spin and orbital vectors of order parameters, the NMR of continuous wave drive is a perfect tool which can be used to detect the pseudo-random lattice of spin soliton of 1D nexus network.³⁶

When the PdB superfluid is equilibrium, the spin magnetization has equilibrium value $\mathbf{S}^{(0)}$ over the system. If the weak homogeneous magnetic drive is turned on, the spin magnetization gets a tiny variation $\delta\mathbf{S}(\mathbf{r}, t)$, where \mathbf{r} and t are spatial and time coordinates respectively. In this perturbed system, the transverse spin magnetization δS_+ may be expanded as

$$\delta S_+(\mathbf{r}, t) = \int d\sigma' \int dt' \frac{\delta S_+}{\delta H_a}(\mathbf{r}, t, \mathbf{r}', t') \delta H_a(\mathbf{r}', t') + O(\delta H_a^2), \quad (37)$$

where $\delta H_a \equiv \delta \mathbf{H}$ with $a = 1, 2, 3$ are the homogeneous weak magnetic drive and a is spatial coordinate indexes. Thus the PdB superfluid under magnetic drive is a linear response system if $|\delta \mathbf{H}| \ll |\mathbf{H}_0|$.⁵² The poles of the transverse spin dynamic response function $\delta S_+/\delta H_a$ correspond to eigen modes of the NMR. We calculate these eigen modes for pseudo-random lattices of inseparable and separable spin solitons with topological invariant 2/4 in this sections.

A. Equation of spin dynamic response under homogeneous continuous-wave drive

Spin orbit coupling play an important role in the NMR measurements of significant properties of different superfluid phases in Helium-3 system. This is because the coherence of superfluid states, which break relative symmetry between spin and orbital degree of freedom of order parameters in superfluid Helium-3, strengthens the SOC energy.^{53,54} This gives rise to the observable NMR frequency shift of nuclear spin magnetization. In our case, the SOC energy takes into account all the information and effects of spin vectors in spin solitons which connect to the KLS domain wall via 1D nexus. Then the existence of spin solitons could lead to the observable frequency shifts in nuclear magnetic resonance spectrum. As a result, what we need to calculate is the spin dynamic response function $\delta S_+/\delta H_a$ dominated by SOC energy.

In this subsection, we utilize the spin dynamic equations dominated by SOC energy to get $\delta S_+/\delta H_a$ as well as its corresponding eigen-equations of poles.⁵⁵ Because the SOC energy is much smaller than the microscopic energy scales of PdB superfluid i.e., Δ_P , the characteristic time scales of spin dynamic response function $\delta S_+/\delta H_a$ is much longer than the time scales of microscopic processes which are proportional to Δ_P^{-1} . All the microscopic processes with time scales Δ_P^{-1} are equilibrium in the spin dynamic processes under weak magnetic drive. This means the spin dynamic equations are a system of hydrodynamic equations of spin magnetization δS_α and spin vectors of order parameter.^{36,55}

In the limit of hydrodynamics, the system of dynamic equations of spin magnetization S_α and spin vectors are system of Liouville equations

$$\frac{\partial S_\alpha}{\partial t} = \{F_{hydrodynamics}, S_\alpha\}, \quad \frac{\partial V_\alpha^a}{\partial t} = \{F_{hydrodynamics}, V_\alpha^a\}, \quad V_\alpha^a = \hat{e}_\alpha^1, \hat{e}_\alpha^2, \hat{d}_\alpha, \quad (38)$$

where $\alpha = 1, 2, 3$ are the indexes of spatial coordinate. And V_α^a denote the three spin vectors of order parameter i.e., $V_\alpha^1 = \hat{e}_\alpha^1$, $V_\alpha^2 = \hat{e}_\alpha^2$, $V_\alpha^3 = \hat{d}_\alpha$. The hydrodynamic free energy of PdB superfluid dominated by SOC energy is

$$F_{hydrodynamics} = \int_\Sigma (f_H + f_{soc} + f_{grad}) d\Sigma. \quad (39)$$

Thus Eq. (38) can be further written as

$$\frac{\partial S_\alpha}{\partial t} = \int_\Sigma d^3 r' \frac{\delta F_{hydrodynamics}}{\delta S_\beta} (r') \{S_\beta(r'), S_\alpha(r)\} + \int_\Sigma d^3 r' \frac{\delta F_{hydrodynamics}}{\delta V_\beta^a} (r') \{V_\beta^a(r'), S_\alpha(r)\}, \quad (40)$$

and

$$\frac{\partial V_\alpha^a}{\partial t} = \int_\Sigma d^3 r' \frac{\delta F_{hydrodynamics}}{\delta S_\beta} (r') \{S_\beta(r'), V_\alpha^a(r)\}, \quad (41)$$

where $\beta = 1, 2, 3$ are indexes of spatial components of hydrodynamic variables. The Poisson brackets between S_α and V_α^a can be gotten by the commutators-based methods in Ref.⁵⁶ as

$$\{S_\alpha(r_1), S_\beta(r_2)\} = \epsilon_{\alpha\beta\gamma} S_\gamma \delta(r_1 - r_2), \quad \{S_\alpha(r_1), V_\beta^a(r_2)\} = \epsilon_{\alpha\beta\gamma} V_\gamma^a \delta(r_1 - r_2), \quad (42)$$

where r_1 and r_2 are the spatial coordinates and $\epsilon_{\alpha\beta\gamma}$ is the Levi-Civita symbol. After plugging Eq. (42) in to Eq. (40) and Eq. (41), the coupled first order dynamic differential equations of spin magnetization S_α and V_α^a are given as

$$\frac{\partial S_\alpha}{\partial t} = \gamma H_\beta \epsilon_{\alpha\beta\gamma} S_\gamma - \frac{3}{5} g_D^2 V_j^d V_\gamma^b \epsilon_{\alpha\beta\gamma} Q_{\beta j}^{bd} + (\partial_i \partial_j V_\beta^a) \epsilon_{\alpha\beta\gamma} K_{ij}^{ba} \quad (43)$$

$$\frac{\partial V_\alpha^a}{\partial t} = \gamma H_\beta \epsilon_{\alpha\beta\gamma} V_\gamma^a - \delta \gamma^2 \chi_\perp^{-1} S_\eta V_\eta^3 V_\beta^3 \epsilon_{\alpha\beta\gamma} - \gamma^2 \chi_\perp^{-1} S_\beta \epsilon_{\alpha\beta\gamma} V_\gamma^a, \quad (44)$$

where $\delta = (\chi_\perp - \chi_\parallel)/\chi_\parallel$ in which χ_\perp and χ_\parallel are the transverse magnetic susceptibility and the longitude magnetic susceptibility of PdB phase respectively.

$$K_{ij}^{ba} = K_1 \delta_{ij} X_m^b X_m^a + K_2 X_j^a X_i^b + K_3 X_j^b X_i^a, \quad Q_{\beta j}^{bd} = X_\beta^b X_j^d + X_\beta^d X_j^b \quad (45)$$

with

$$X_i^1 = \Delta_{\perp 1} \hat{x}_i, \quad X_i^2 = \Delta_{\perp 2} \hat{y}_i, \quad X_i^3 = \Delta_{\parallel} \hat{z}_i. \quad (46)$$

The details of calculation from Eq. (40) to Eq. (44) are shown in appendixes Sec. B 1.

Based on the first order equations of spin magnetization and degenerate parameters in Eq. (43) and Eq. (44), we can further derive the second order spin dynamic response equations of δS_α under weak magnetic drive δH_α . This was done by plugging in $S_\alpha = S_\alpha^{(0)} + \delta S_\alpha(\mathbf{r}, t)$, $V_\alpha^a = V_\alpha^{a(0)} + \delta V_\alpha^a(\mathbf{r}, t)$ and $H_\alpha = H_\alpha^{(0)} + \delta H_\alpha(t)$ in to Eq. (43) and Eq. (44). Here the $S_\alpha^{(0)}$ and $V_\alpha^{a(0)}$ are the equilibrium spin magnetization and equilibrium degenerate parameters respectively. While the $\delta S_\alpha(\mathbf{r}, t)$ and $\delta V_\alpha^a(\mathbf{r}, t)$ are the dynamic parts of the perturbed spin magnetization and degenerate parameters. The $H_\alpha^{(0)}$ is the static magnetic field and $\delta H_\alpha(t) = |\delta \mathbf{H}| \hat{x} e^{-i\omega t}$ is the homogeneous RF continuous-wave drive. We put the details of calculations in appendixes Sec. B 2 and the derived spin dynamic response equations within frequency form is

$$i\omega \delta S_\alpha(\omega) = \gamma \epsilon_{\alpha\beta\gamma} H_\beta^{(0)} \delta S_\gamma(\omega) + \gamma \epsilon_{\alpha\beta\gamma} S_\gamma^{(0)} \delta H_\beta(\omega) + \frac{\Xi_{\alpha\lambda}}{i\omega} \delta S_\lambda(\omega) + \frac{C_{\alpha\eta}}{i\omega} \delta H_\eta(\omega) \quad (47)$$

and

$$\begin{aligned} \Xi_{\alpha\lambda} &= \frac{\gamma^2}{\chi_\perp} K_{ij}^{ba} \Lambda_{ij\alpha\lambda}^{ba} + \frac{6g_D\gamma^2}{5\chi_\perp} R_{j\lambda\alpha\beta}^{db} Q_{\beta j}^{bd} + \frac{6g_D\gamma^2}{5\chi_\perp} V_{\zeta 0}^d V_{\gamma 0}^b \epsilon_{j\lambda\zeta} \epsilon_{\alpha\beta\gamma} Q_{\beta j}^{bd} \\ C_{\alpha\eta} &= \gamma G_{ij\alpha\eta}^{ba} K_{ij}^{ba} - \frac{6g_D\gamma}{5} R_{j\eta\alpha\beta}^{db} Q_{\beta j}^{bd} - \frac{6g_D\gamma}{5} V_{\zeta 0}^d V_{\gamma 0}^b \epsilon_{j\eta\zeta} \epsilon_{\alpha\beta\gamma} Q_{\beta j}^{bd}, \end{aligned} \quad (48)$$

where

$$\begin{aligned} R_{j\eta\alpha\beta}^{db} &= V_j^{d(0)} V_\beta^{b(0)} \delta_{\eta\alpha} - V_j^{d(0)} V_\alpha^{b(0)} \delta_{\eta\beta}, \\ G_{ij\alpha\gamma}^{ba} &= (\partial_i \partial_j V_\alpha^{b(0)}) V_\gamma^{a(0)} - (\partial_i \partial_j V_\beta^{b(0)}) \delta_{\beta\gamma} V_\alpha^{a(0)}, \\ \Lambda_{ij\alpha\lambda}^{ba} &= (\partial_i \partial_j V_\beta^{b(0)}) \delta_{\beta\lambda} V_\alpha^{a(0)} + (V_\gamma^{b(0)} V_\gamma^{a(0)} \delta_{\alpha\lambda} - \delta_{\gamma\lambda} V_\alpha^{b(0)} V_\gamma^{a(0)}) \partial_i \partial_j \\ &\quad + [(\partial_i V_\gamma^{b(0)}) V_\gamma^{a(0)} \delta_{\alpha\lambda} - (\partial_i V_\alpha^{b(0)}) V_\gamma^{a(0)} \delta_{\gamma\lambda}] \partial_j \\ &\quad + [\partial_j V_\gamma^{b(0)} V_\gamma^{a(0)} \delta_{\alpha\lambda} - (\partial_j V_\alpha^{b(0)}) V_\gamma^{a(0)} \delta_{\gamma\lambda}] \partial_i \\ &\quad + \delta_{\gamma\lambda} (\partial_i \partial_j V_\alpha^{b(0)}) V_\gamma^{a(0)}. \end{aligned} \quad (49)$$

The first two terms of Eq. (47) correspond to the NMR response of Larmor precession of δS_α with frequency $\omega_L = \gamma H^{(0)}$. While the last two terms of Eq. (47) induce the NMR frequency shift. From Eq. (48) and Eq. (49), we found all the NMR frequency shifts are induced by the equilibrium textures of spin vectors. In our case of pseudo-random lattices of spin solitons with topological invariant 2/4, the NMR frequency shifts are totally induced by equilibrium textures of spin solitons. That why the transverse NMR spectrum is perfect tool to observe the 1D nexus network. Taking into account the static magnetic field $\mathbf{H}^{(0)} = |\mathbf{H}^{(0)}| \hat{\mathbf{y}}$ and the parametrization Eq. (10), we can derive the dynamic response equations of transverse spin magnetization $\delta S_+ = [\delta S_1(\omega) + i\delta S_3(\omega)]/\sqrt{2}$ under weak magnetic drive $\delta \mathbf{H}(t)$, see the detail of calculation in appendixes Sec. B 3. This calculation gives

$$(\omega^2 - \omega_L^2) \delta S_+(\omega) = (\Xi_{11} + \Xi_{33}) \delta S_+(\omega) + i(\Xi_{13} - \Xi_{31}) \delta S_+(\omega) - \frac{1}{2} (C_{11} + C_{31}) \delta H_1(\omega) - \frac{\chi_\perp}{\sqrt{2}\gamma} (\Xi_{33} + i\Xi_{13} - i\Xi_{31}) \delta H_1(\omega). \quad (50)$$

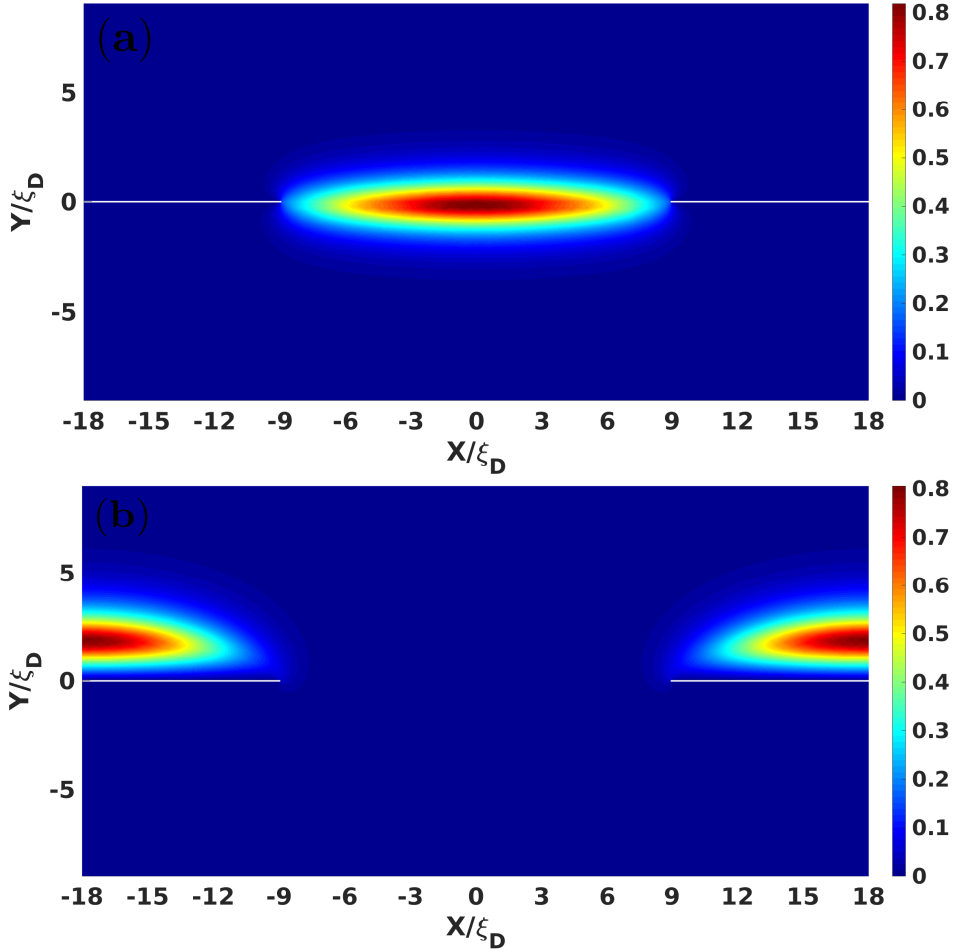


FIG. 8: The modulus $|\delta S_+(\omega)|$ of the lowest transverse spin dynamic response modes located in the unit cells of pseudo-random lattices of inseparable and separable 2/4 spin solitons. In both cases, we depict the results with parameters $|q| = 0.18$ and $D = 18\xi_D$. (a) $|\delta S_+(\omega)|$ in unit cell consists of inseparable spin solitons (π -solitons); (b) $|\delta S_+(\omega)|$ in unit cell consists of separable spin solitons (KLS-solitons and Solitons) lattices.

Thus

$$\frac{\delta S_+(\omega)}{\delta H_1(\omega)} \propto \frac{1}{\omega^2 - \omega_L^2 - (\Xi_{11} + \Xi_{33}) - i(\Xi_{13} - \Xi_{31})}. \quad (51)$$

The poles of spin dynamic response function $\delta S_+/\delta H_1$, which are determined by eigen-equation

$$(\omega^2 - \omega_L^2)\delta S_+(\omega) = (\Xi_{11} + \Xi_{33}) + i(\Xi_{13} - \Xi_{31})\delta S_+(\omega), \quad (52)$$

correspond to the eigen-modes of transverse NMR spectrum in the presence of pseudo-random lattices of spin solitons. We numerically solve this eigen-equation in next subsection with different D and $|q|$.

B. NMR frequency shift and ratio intensity of pseudo-random lattice consist of inseparable and separable spin soliton

Firstly we transform the eigen-equation of transverse NMR modes into dimensionless form, which is suitable for the numeric calculation. All $\Xi_{\alpha\lambda}$ operators in Eq. (52) must be calculated with parametrization Eq. (10), See the details in appendices Sec. B 4. This gives

$$\lambda\delta S_+(\omega) = \xi_D^2[(6\rho_2^2 + \rho_1^2 + 1)\partial_y\partial_y + (3\rho_1^2 + 2\rho_2^2 + 1)\partial_x\partial_x - 2iV]\delta S_+(\omega) + U\delta S_+(\omega) \quad (53)$$

with

$$V = (1 + 3\rho_1^2 \cos 2\theta) \partial_x \theta \partial_x + (1 + \rho_1^2) \partial_y \theta \partial_y + \frac{1}{2} [(1 + \rho_1)^2 \sin 2\theta - (1 + \rho_1) \rho_2 \cos \theta], \quad (54)$$

$$U = (1 + \rho_1) [-(1 + \rho_1) \cos 2\theta - 5\rho_2 \sin \theta] + 1 + \rho_1^2 + 4\rho_2^2, \quad (55)$$

where $\rho_1 = \Delta_{\perp 1} / \Delta_P$ and $\rho_2 = \Delta_{\perp 2} / \Delta_P$. Here the dimensionless eigen-value

$$\lambda = \frac{(\omega^2 - \omega_L^2)}{\tilde{\Omega}^2} \quad (56)$$

is the transverse NMR frequency shift under weak magnetic drive and

$$\tilde{\Omega}^2 = \frac{5\chi_{\perp}}{6\gamma^2 \Delta_P^2 g_D}. \quad (57)$$

We use the Galerkin strategy under finite-element partition to solve Eq. (53).⁵⁷ The solving regions are identical with the unit cells of pseudo-random lattices of spin solitons. The equilibrium spin textures of pseudo-random lattices of inseparable and separable spin solitons, which we have gotten in Sec. IV C, are directly used to solve Eq. (53). Because the magnetic drive δH_{α} is low energy drive, we just consider the spin dynamic response mode with lowest λ of Eq. (53). Moreover, the ratio intensity of NMR signal is other observable beside the frequency shift λ . The surface density of ratio intensity which is generated by unit area of pseudo-random lattices of spin solitons is

$$n \cdot \frac{|I_{\delta S_+}|^2}{I_{\delta S_+}^2} = n \cdot \frac{|\int_{\Sigma} \delta S_+ d\Sigma|^2}{\int_{\Sigma} |\delta S_+|^2 d\Sigma}, \quad (58)$$

where $n = (D)^{-2}$ is the density of 1D nexus.

In Fig. 8, we demonstrate the modulus of the lowest transverse spin dynamic response modes $|\delta S_+(\omega)|$ located in the unit cells of pseudo-random lattices of inseparable and separable 2/4 spin solitons. The transverse NMR frequency shifts λ and surface densities of ratio intensity of pseudo-random lattices for inseparable and separable 2/4 spin solitons are shown in Fig. 9 and Fig. 10 respectively. Let us consider them separately.

1. *Transverse NMR frequency shifts and surface densities of ratio intensity of pseudo-random lattices consist of inseparable spin solitons*

The Transverse NMR frequency shifts λ of pseudo-random lattices of inseparable spin solitons (π -solitons) exactly coincides with the experimentally observed values in ref.³⁵. As been shown in Fig. 9 (a), the numeric values of λ generated by pseudo-random lattices consist of π -solitons is around -1.01 to -1.03 when pseudo-random lattice model is good enough i.e., $D \geq 10\xi_D$. In this case, the transverse NMR frequency shifts λ slightly increase as $|q|$ increasing when $|q| > 0.16$. This phenomenon has also been observed in experiment of ref.³⁵. The ratio intensities generated by per unit area of pseudo-random lattice consist of π -solitons linearly increase when the square root of angular velocity $\sqrt{\Omega}$ increases, as shown in Fig. 9 (d). This coincides with the $\sqrt{\Omega}$ -scaling of satellite intensity observed in the experiment when $T = 0.38T_c$ ($|q| \approx 0.152$).³⁵

In Sec. IV C 2, we found the possible equilibrium state which was observed in experiment is the pseudo-random lattices of 2/4 inseparable spin solitons. Here we see the results of numeric simulations of transverse NMR spin dynamic response of this kind of pseudo-random lattices indeed coincide with the experimental observations.

2. *Transverse NMR frequency shifts and surface densities of ratio intensity of pseudo-random lattices consist of separable spin solitons*

In contrast with pseudo-random lattices consist of inseparable 2/4 spin solitons, the transverse NMR frequency shifts of pseudo-random lattices consist of separable spin solitons strongly deviate against the results of experimental observations, see Fig. 10 (a). λ generated by pseudo-random lattice of separable spin solitons increase when $|q|$ increases. This is because only the soliton spin textures with $|\Delta\theta| = \pi - 2\theta_0$ of separable spin solitons contributes to the transverse NMR frequency shift, and the frequency shifts λ of the soliton textures with $|\Delta\theta| = \pi - 2\theta_0$ increase as $|q|$ increases, see the details in appendices Sec. C. Moreover, the magnitudes of the surface densities of ratio intensity $n \cdot (|I_{\delta S_+}|^2 / I_{\delta S_+}^2)$ generated by pseudo-random lattices of separable spin solitons are larger than these generated by pseudo-random lattices consist of inseparable spin solitons, as shown in Fig. 10 (d).

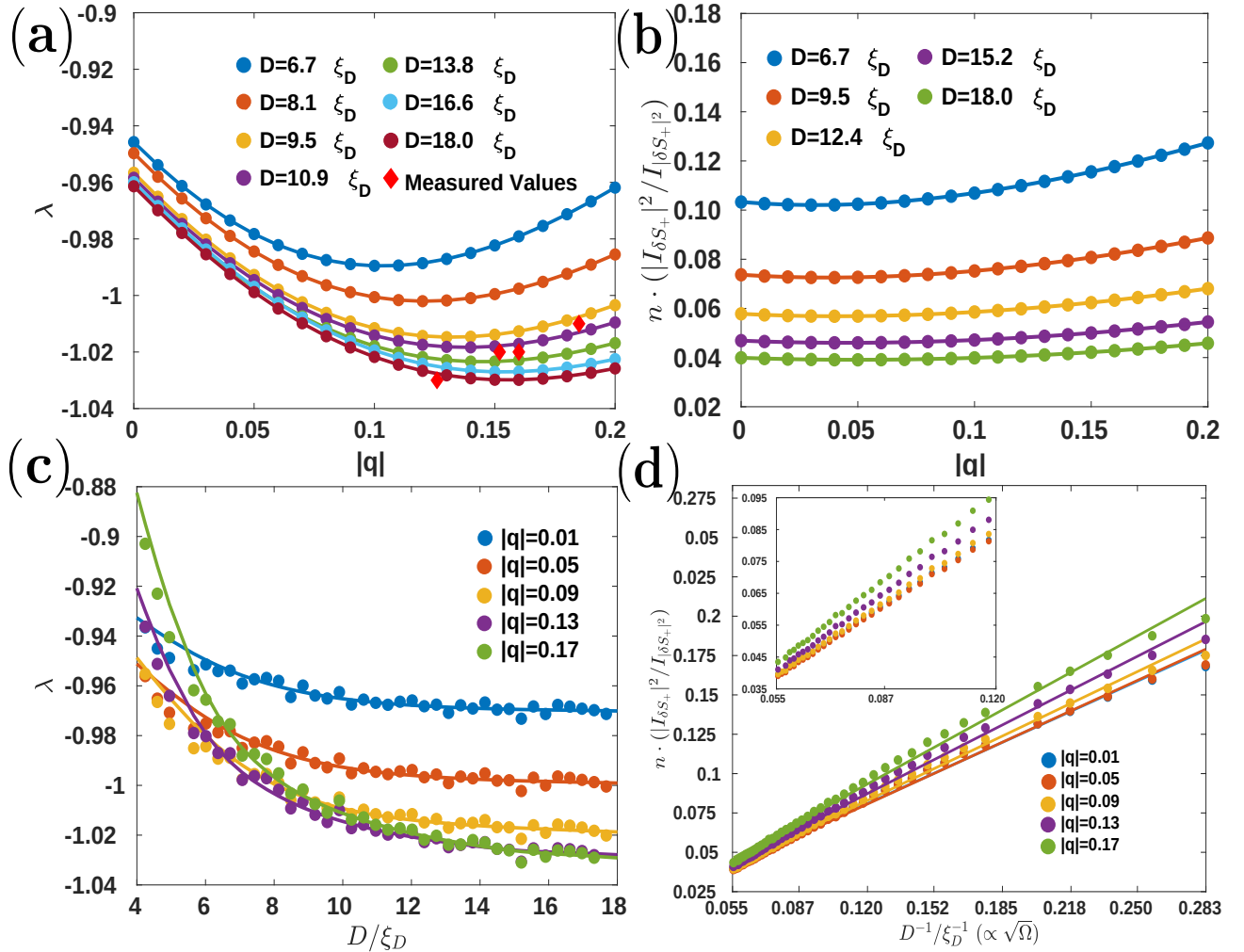


FIG. 9: Transverse NMR frequencies shifts λ and surface densities of ratio intensity $n \cdot (|I_{\delta S_+}|^2 / I_{|\delta S_+|^2})$ of pseudo-random lattices consist of inseparable spin solitons (π -solitons). The frequency shifts λ are eigen-values of eigen-equation Eq. (53) with equilibrium textures of π -solitons in London limit. The surface densities of NMR ratio intensity are calculated by using Eq. (58). All scattering dots represent the original numeric results, while colored lines are smoothing spline fittings of these original numeric results. (a) Transverse frequency shifts λ as functions of $|q|$ with different D . For large enough unit cells ($D > 10\xi_D$), we found λ decreases when $|q|$ increases as $|q| \leq 0.16$. The typical values of λ are around -1.015 to -1.03 when pseudo-random lattices model is good enough i.e., $D \geq 10\xi_D$. This exactly coincides with the region of λ which was observed in experiment of ref.³⁵, as shown via red diamonds. (b) depicts the surface densities of ratio intensity $n \cdot (|I_{\delta S_+}|^2 / I_{|\delta S_+|^2})$ of the eigen-mode of λ . (c) depicts the transverse frequency shifts λ as function of D . (d) The surface densities of ratio intensity $n \cdot (|I_{\delta S_+}|^2 / I_{|\delta S_+|^2})$ as function of $1/D \propto \sqrt{\Omega}$. We found $n \cdot (|I_{\delta S_+}|^2 / I_{|\delta S_+|^2})$ increases linearly if $\sqrt{\Omega}$ increases. This coincides with the results of experimental observation in ref.³⁵. The inset is the magnified plot between $|q| = 0.055$ till $|q| = 0.120$.

VI. THE MIRROR SYMMETRY IN THE PRESENCE OF 1D NEXUS AND ITS BREAK

As we mentioned before, The London limit free energy $F(\theta)_{London}$ has a mirror symmetry when the coordinates are permuted to each other i.e., $F[\theta(x', y')] = F[\theta(x, y)]$ with $x' = y$ and $y' = x$. This symmetry does not vanish even in the presence of 1D nexus. As a result, the spin textures of 2/4 spin solitons have this mirror symmetry as well.

This discrete symmetry originates from the reduction of degenerate space of order parameter by requirement of continuity of order parameter in the presence of KLS string wall. To understand this, we start from the degenerate space of PdB which generates from transition of polar phase vacuum. In this case, $R_{PdB} \cong SO(2)_{S-L} \times \mathbb{Z}_2^{S-\Phi}$, in which the non-trivial element of \mathbb{Z}_2 corresponds to the presence of KLS domain wall.³⁷ In the presence of KLS domain wall, the requirement of continuity of limit of order parameter reduces the degenerate space of \hat{e}^1 and \hat{e}^2 on both sides of domain wall from $SO(2)_{S-L}$ to (i) $\hat{e}^1 \rightarrow -\hat{e}^1$, while \hat{e}^2 keeps its direction and (ii) $\hat{e}^2 \rightarrow -\hat{e}^2$, while \hat{e}^1 keeps

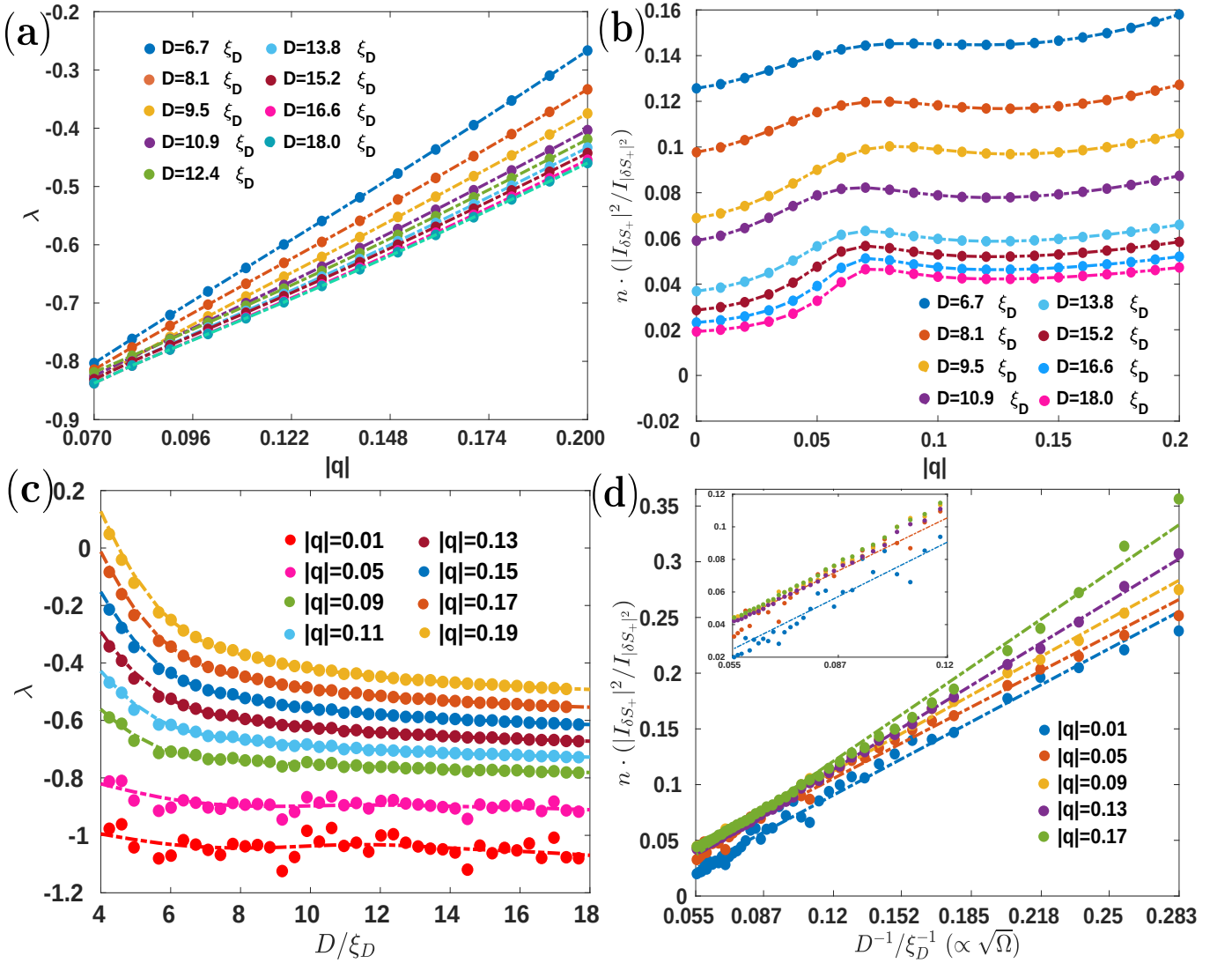


FIG. 10: Transverse NMR frequencies shifts λ and surface densities of ratio intensity $n \cdot (|I_{\delta S_+}|^2 / I_{|\delta S_+|^2})$ of pseudo-random lattices consist of separable spin solitons (KLS-solitons and solitons). The frequency shifts λ are eigen-values of eigen-equation Eq. (53) with equilibrium textures of $1/4 + 1/4$ spin soliton in London limit. The surface densities of NMR ratio intensity are calculated by using Eq. (58). All scattering dots represent the original numeric results, while colored lines are smoothing spline fittings of these original numeric results. (a) Transverse NMR frequency shifts λ increases when $|q|$ increases. This is because only solitons with $|\Delta\theta| = \pi - 2\theta_0$ contribute to the lowest transverse spin dynamic response mode. When $|q|$ increases, λ generated by solitons increases, see the details in appendices Sec. C. The typical values of λ are larger than -0.9 when pseudo-random lattices model is good enough i.e., $D \geq 10\xi_D$. (b) depicts the surface densities of ratio intensity $n \cdot (|I_{\delta S_+}|^2 / I_{|\delta S_+|^2})$ of the eigen-mode of λ . (c) depicts the transverse frequency shifts λ as function of D . (d) The surface densities of ratio intensity $n \cdot (|I_{\delta S_+}|^2 / I_{|\delta S_+|^2})$ as function of $1/D \propto \sqrt{\Omega}$. The inset is the magnified plot between $|q| = 0.055$ till $|q| = 0.120$.

its direction. The parametrization in Eq. (10), which we used in previous calculations and discussions, corresponds to the case (i) and the direction of static magnetic field $\mathbf{H}^{(0)}$ is set to parallel with the $\hat{\mathbf{e}}^2$. Because the case (ii) is another possible vacuum state with same free energy of case (i) in the presence of KLS domain wall, the London limit free energy $F(\theta)_{London}$ is invariant when we transform from vacuum state (i) to vacuum state (ii). In our case, the parametrization of vacuum state (ii) is

$$\hat{\mathbf{d}} = \hat{y}\cos\theta - \hat{z}\sin\theta, \quad \hat{\mathbf{e}}^2 = -\hat{y}\sin\theta - \hat{z}\cos\theta, \quad \hat{\mathbf{e}}^1 = \hat{x}, \quad \mathbf{H}^{(0)} = H\hat{x}, \quad (59)$$

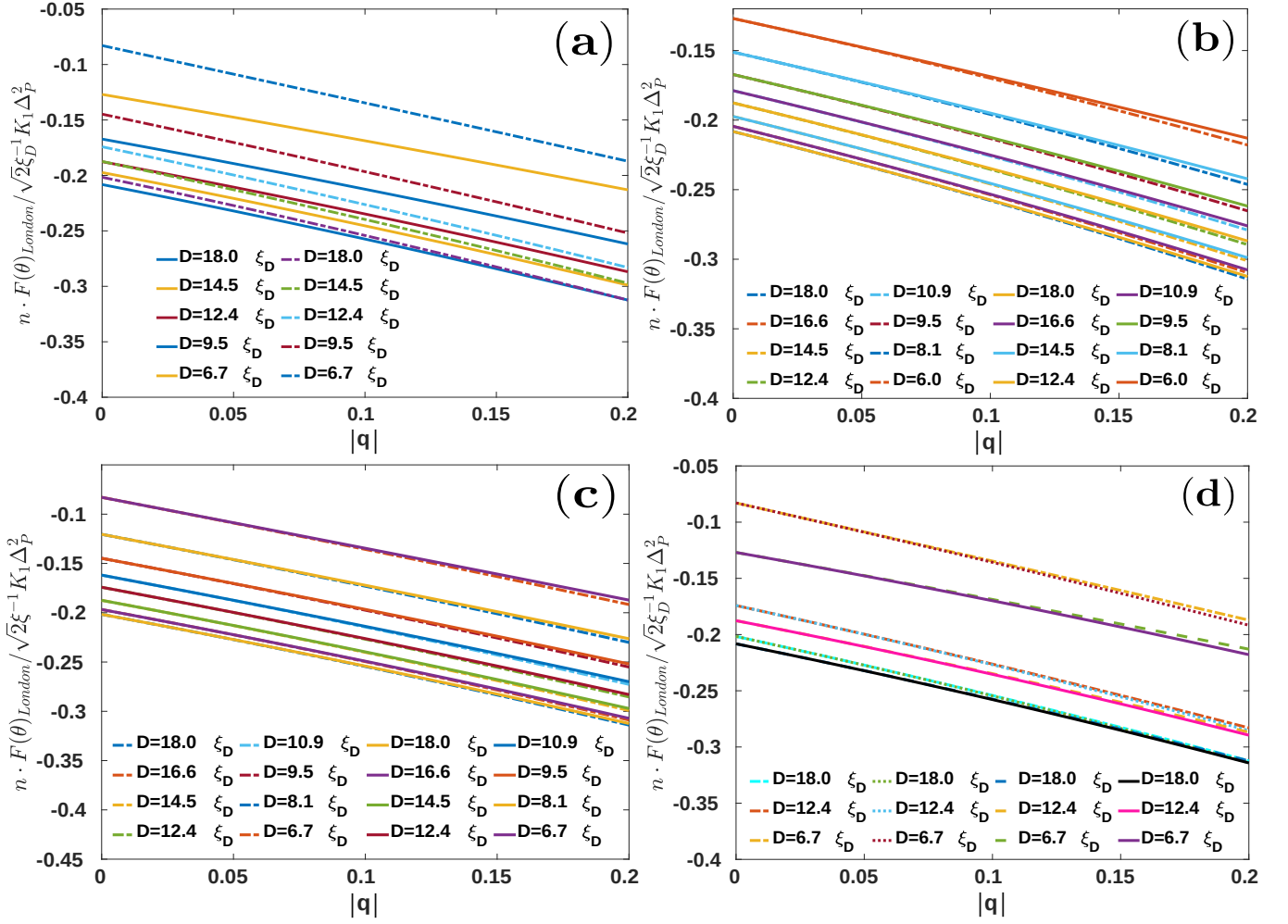


FIG. 11: Surface densities of equilibrium London limit free energies of pseudo-random lattices consist of inseparable and separable 2/4 spin solitons of vacuum state (i) and vacuum state (ii) respectively. These two vacuum states are not degenerated with same free energy any more when the direction of KLS domain wall is fixed. (a) The surface densities of London limit free energies of pseudo-random lattices consist of inseparable spin solitons (π -solitons) and separable spin solitons (KLS-solitons and solitons) in the vacuum state (ii). This figure shows identical features with Fig. 7(c). (b) depicts the surface densities of London limit free energies of pseudo-random lattices consist of inseparable 2/4 spin solitons of vacuum states (i) and (ii) respectively. The dash-dot lines represent the vacuum state (i) while the solid lines represent the vacuum state (ii). (c) depicts the surface densities of London limit free energies of pseudo-random lattices consist of separable 2/4 spin solitons of vacuum states (i) and (ii) respectively. The dash-dot lines represent the vacuum state (i) while the solid lines represent the vacuum state (ii). (d) depicts the surface densities of London limit free energies of pseudo-random lattices of 2/4 spin solitons in vacuum states (i) and (ii). The solid lines and dash lines represent the pseudo-random lattices consist of inseparable spin solitons (π -solitons) within vacuum states (i) and (ii) respectively. The dot lines and dash-dot lines represent the pseudo-random lattices consist of separable spin solitons (KLS-solitons and solitons) within vacuum states (i) and (ii) respectively. We found the pseudo-random lattices consist of 2/4 inseparable spin solitons within vacuum state (i) have lowest equilibrium free energies.

and the corresponding dimensionless London limit free energy is

$$\tilde{F}(\theta)_{London} = \frac{1}{\xi_D} \int_{\Sigma} \left[\frac{1}{2} (\gamma_1 + 2\gamma_2) \partial_y \theta \partial_y \theta + \frac{1}{2} \gamma_1 \partial_x \theta \partial_x \theta + \frac{1}{\xi_D^2} \left(-\frac{1}{2} \cos 2\theta - \gamma_3 \sin \theta \right) \right] d\Sigma \quad (60)$$

where

$$q = \frac{\Delta_{\perp 1}}{\Delta_P}, \quad \gamma_1 = 1 + |q|^2, \quad \gamma_2 = |q|^2, \quad \gamma_3 = q(1 + |q|). \quad (61)$$

Comparing Eq. (60) and Eq. (28), we can see the mirror symmetry.

However, this discrete symmetry may be destroyed if the direction of domain wall is fixed. In this case, the term containing γ_3 is invariant for both parametrizations, and thus violates this mirror symmetry. As a result, the equilibrium states of Eq. (60) and Eq. (28) are not identical any more. Then we need to check the equilibrium London limit free energy of these two different equilibrium states. We did the same numeric minimizations of London limit free energy with parametrization Eq. (59) and calculated the surface densities of equilibrium free energies of pseudo-random lattices of spin solitons in vacuum state (ii). The latter can be evaluated as

$$n \cdot \tilde{F}(\theta)_{London|(ii)} \sim \frac{1}{8}(1+|q|^2) \frac{\pi^2}{\xi_D D} + \frac{\pi^2}{4\xi_D D} |q|^2 + \frac{5}{12\xi_D^2 g_D \Delta_P^2} [f_{soc|y>0} + f_{soc|y<0}]_q \sim n \cdot \tilde{F}(\theta)_{London|(i)} + \frac{\pi^2}{4\xi_D D} |q|^2. \quad (62)$$

Then we can expect the surface densities of equilibrium London limit free energy of vacuum state (ii) are slightly higher than those of vacuum state (i) when $|q| \leq 0.2$. In Fig. 11, we show this for pseudo-random lattices consist of inseparable and separable $2/4$ spin solitons of vacuum states (i) and (ii) respectively. In all cases, the surface densities of London limit free energy of vacuum state (ii) are indeed a little bit higher than those of vacuum state (i).

VII. CONCLUSIONS AND DISCUSSIONS

In this work, we discussed the topological origin of the novel 1D nexus objects in PdB phase of nafen-distorted Helium-3 superfluid system. The topological objects named 2D nexus objects which is similar but has higher spatial dimension are predicted in PdB superfluid.³⁷ This object is formed by connection between vortex skyrmion of $\hat{\mathbf{d}}$ vector and spin vortices of $\hat{\mathbf{e}}^1$ and $\hat{\mathbf{e}}^2$ vectors via monopole. Earlier vortex skyrmions formed by phase and orbital degenerate parameters have been suggested and observed in Helium-3 A-phase^{59–63}, it also probably be observed in spin and orbital degree of freedom of 2D nexus in PdB phase. In contrast to the out of observation of 2D nexus objects, the 1D nexus objects are observed directly in the continuous wave NMR spectrum in the rotating PdB sample.³⁵ There are two reasons making this possible.

One reason is the pinning effect of nafen-strands. This strong pinning fixes the locations of the HQVs once they appear during cooling down with a given angular velocity. In the limit of low angular velocity i.e., $\Omega \ll \Omega_c$, the average distance between pinned HQVs is around hundred microns. As a result, the KLS domain walls attached on the HQVs have very large geometric sizes when the symmetry break transition from polar phase to PdB phase occurs. In the spatial regions with length scales ξ_D , the SOC energy reduces the vacuum manifolds to discrete sets. The reduced vacuum manifolds have spin solitons which are described by relative homotopy group $\pi_1(R_1^H, \tilde{R}_1^{SOC})$. Similar process also happen in bulk Helium-3 superfluid and spinor Bose condensate.^{46,47,58} We demonstrated the the subgroup G of $\pi_1(R_1^H, \tilde{R}_1)$, which describes the spin solitons with topological invariant $2/4$, is isomorphic to the group M which describes the spin degree of freedom of KLS string wall. This fact suggests that HQV is 1D nexus which smoothly connect the spin solitons and KLS domain wall.

The other reason is the textures of $2/4$ spin solitons with length scales ξ_D can strongly influence the SOC energy and then modify the low frequency spin dynamic response of the spin densities under continuous wave drive.

In the nafen-distorted Helium-3 superfluid, the 1D nexus objects connect with each other via large size KLS domain wall and then form network. The $2/4$ spin solitons connected on every KLS string wall form pseudo-random lattices in the absence of coupling between spin solitons. We discussed the equilibrium configurations and the surface densities of equilibrium free energies of two different pseudo-random lattices consist of spin solitons with topological invariant $2/4$. These two types of pseudo-random lattices correspond to two representations of group $G = \pi_1(S_S^1, \tilde{R}_2)$, the relative homotopy group of $2/4$ spin solitons. Our analysis shows the pseudo-random lattices consist of inseparable spin solitons are energy favorable. To compare with the experimental observations, we further calculated the transverse spin dynamic response under continuous wave drive. The resulted NMR frequency shifts of pseudo-random lattices consist of inseparable spin solitons exactly coincide with the experimental measurements. The explicitly break of mirror symmetry in the presence of KLS domain wall is also be considered.

In the limit of low angular velocity, the pseudo-random lattices models work very well because the randomness of the network of 1D nexus objects doesn't influence the spin textures of spin solitons. Thus we can not find any observable effect originated from this randomness. However, when the angular velocity approaches the critic value Ω_c , the coupling between spin solitons can dramatically change the equilibrium spin textures of random lattices of spin solitons. In this case, the random distributions of KLS string wall lead to spin solitons glasses. Thus we can expect the observable effects of this randomness on the NMR spectrums under high enough angular velocity. Moreover, PdB phase could be a good platform to observe the monopole-antimonopole networks because the string monopole is topologically protected by π_2 relative homotopy group.³⁷ These kinds of complex networks are predicted in condensed matter system and also in the Grand Unified Theories.^{64–67} In the absence of magnetic field, the string monopoles in PdB phase may connect to planar solitons with geometric size around ξ_D because of the reduction of vacuum manifold

by SOC energy. Similar with pseudo-random lattices of spin solitons, these planar solitons may result in observable influence on NMR spectrum.

Acknowledgments

We thank helpful and constructive discussions and comments from Grigory. E. Volovik, Jaakko Nissinen, Vladislav Zavyalov and Erkki. V. Thuneberg. We also especially thank Vladimir B. Eltsov, Jere. T. Mkinen and Juho. Rysti for helpful discussions and comments about experiments of polar distorted B-phase. This work has been supported by the European Research Council (ERC) under the European Unions Horizon 2020 research and innovation programme (Grant Agreement No. 694248).

Appendix A: Pseudo-random lattices consist of separable spin solitons with two different domain wall boundary conditions – $\theta_{KLS} = 0$ and $\theta_{KLS} = \pi$

To show the equivalence of equilibrium configurations of pseudo-random lattices between boundary conditions $\theta_{KLS} = 0$ and $\theta_{KLS} = \pi$, we calculated the spin textures of one-half unit cell of the lattices consist of separable spin solitons with topological invariant $1/4 + 1/4$ under these two boundary conditions. Based on the resulted equilibrium spin texture, the London limit free energies of one-half unit cell and the surface densities of London limit free energies of the pseudo-random lattices were calculated. In Fig. 12 (a) and (b), we show the equilibrium spin textures of one-half unit cell with $\theta_{KLS} = 0$ and $\theta_{KLS} = \pi$ respectively. We can see these two textures are related by π -rotation about x axis. They have same London limit free energies and same surface densities of London limit free energy as shown in Fig. 12 (c) and (d). These information show the equilibrium spin textures of pseudo-random lattices consist of separable spin solitons with KLS wall boundary conditions $\theta_{KLS} = 0$ and $\theta_{KLS} = \pi$ are identical.

Appendix B: The derivation of spin dynamic response equations

1. The derivation of the first order dynamic equations of spin magnetization and degenerate parameters

Using Eq. (3), Eq. (2), Eq. (4) and Eq. (7), All terms of energy densities in hydrodynamic free energy $F_{hydrodynamics}$ are

$$\begin{aligned}
f_{grad} = & \frac{1}{2} \{ K_1 \Delta_P^2 \partial_i \hat{d}_\alpha \partial_i \hat{d}_\alpha + K_1 \Delta_{\perp 1}^2 \partial_i \hat{e}_\alpha^1 \partial_i \hat{e}_\alpha^1 + K_1 \Delta_{\perp 2}^2 \partial_i \hat{e}_\alpha^2 \partial_i \hat{e}_\alpha^2 \\
& + K_2 \Delta_P^2 \partial_j \hat{d}_\alpha \hat{z}_j \partial_i \hat{d}_\alpha \hat{z}_i + K_2 \Delta_{\perp 1}^2 \partial_j \hat{e}_\alpha^1 \hat{x}_j \partial_i \hat{e}_\alpha^1 \hat{x}_i + K_2 \Delta_{\perp 2}^2 \partial_j \hat{e}_\alpha^2 \hat{y}_j \partial_i \hat{e}_\alpha^2 \hat{y}_i \\
& + K_3 \Delta_P^2 \partial_i \hat{d}_\alpha \hat{z}_i \partial_j \hat{d}_\alpha \hat{z}_j + K_3 \Delta_{\perp 1}^2 \partial_i \hat{e}_\alpha^1 \hat{x}_i \partial_j \hat{e}_\alpha^1 \hat{x}_j + K_3 \Delta_{\perp 2}^2 \partial_i \hat{e}_\alpha^2 \hat{y}_i \partial_j \hat{e}_\alpha^2 \hat{y}_j \\
& + K_2 [\partial_j \hat{d}_\alpha \hat{z}_i \partial_j \hat{e}_\alpha^1 \hat{x}_j + \partial_j \hat{e}_\alpha^1 \hat{x}_i \partial_i \hat{d}_\alpha \hat{z}_j] \Delta_P \Delta_{\perp 1} + K_2 [\partial_j \hat{d}_\alpha \hat{z}_i \partial_i \hat{e}_\alpha^2 \hat{y}_j + \partial_j \hat{e}_\alpha^2 \hat{y}_i \partial_i \hat{d}_\alpha \hat{z}_j] \Delta_P \Delta_{\perp 2} \\
& + K_2 [\partial_j \hat{e}_\alpha^1 \hat{x}_i \partial_i \hat{e}_\alpha^2 \hat{y}_j + \partial_j \hat{e}_\alpha^2 \hat{y}_i \partial_i \hat{e}_\alpha^1 \hat{x}_j] \Delta_{\perp 1} \Delta_{\perp 2} + K_3 [\partial_i \hat{d}_\alpha \hat{z}_i \partial_j \hat{e}_\alpha^1 \hat{x}_j + \partial_i \hat{e}_\alpha^1 \hat{x}_i \partial_j \hat{d}_\alpha \hat{z}_j] \Delta_P \Delta_{\perp 1} \\
& + K_3 [\partial_i \hat{d}_\alpha \hat{z}_i \partial_j \hat{e}_\alpha^2 \hat{y}_j + \partial_i \hat{e}_\alpha^2 \hat{y}_i \partial_j \hat{d}_\alpha \hat{z}_j] \Delta_P \Delta_{\perp 2} + K_3 [\partial_i \hat{e}_\alpha^1 \hat{x}_i \partial_j \hat{e}_\alpha^2 \hat{y}_j + \partial_i \hat{e}_\alpha^2 \hat{y}_i \partial_j \hat{e}_\alpha^1 \hat{x}_j] \Delta_{\perp 1} \Delta_{\perp 2} \},
\end{aligned} \tag{B1}$$

$$\begin{aligned}
f_{soc} = & \frac{3gD}{5} \{ \Delta_P^2 (\hat{d}_i \hat{z}_i)^2 + \Delta_P \Delta_{\perp 1} (\hat{d}_i \hat{z}_i) (\hat{e}_j^1 \hat{x}_j) + \Delta_P \Delta_{\perp 2} (\hat{d}_i \hat{z}_i) (\hat{e}_j^2 \hat{y}_j) + \Delta_P \Delta_{\perp 1} (\hat{e}_i^1 \hat{x}_i) (\hat{d}_j \hat{z}_j) \\
& + \Delta_{\perp 1}^2 (\hat{e}_i^1 \hat{x}_i)^2 + \Delta_{\perp 1} \Delta_{\perp 2} (\hat{e}_i^1 \hat{x}_i) (\hat{e}_j \hat{y}_j) + \Delta_{\perp 2} \Delta_{\perp 1} (\hat{e}_i^2 \hat{y}_i) (\hat{d}_j \hat{z}_j) + \Delta_{\perp 2} \Delta_{\perp 1} (\hat{e}_i^2 \hat{y}_i) (\hat{e}_j^1 \hat{x}_j) + \Delta_{\perp 2}^2 (\hat{e}_i^2 \hat{y}_i)^2 \\
& + \Delta_P^2 (\hat{d}_i \hat{z}_i)^2 + \Delta_P \Delta_{\perp 1} (\hat{d}_i \hat{z}_i) (\hat{e}_j^1 \hat{x}_j) + \Delta_P \Delta_{\perp 2} (\hat{d}_i \hat{z}_i) (\hat{e}_j^2 \hat{y}_j) + \Delta_P \Delta_{\perp 1} (\hat{e}_i^1 \hat{x}_j) (\hat{d}_j \hat{z}_i) + \Delta_{\perp 1}^2 (\hat{e}_i^1 \hat{x}_i)^2 \\
& + \Delta_{\perp 1} \Delta_{\perp 2} (\hat{e}_i^1 \hat{x}_j) (\hat{e}_j^2 \hat{y}_j) + \Delta_{\perp 2} \Delta_P (\hat{e}_i^2 \hat{y}_j) (\hat{d}_j \hat{z}_i) + \Delta_{\perp 1} \Delta_{\perp 2} (\hat{e}_i^2 \hat{y}_j) (\hat{e}_j^1 \hat{x}_i) + \Delta_{\perp 2}^2 (\hat{e}_j^2 \hat{y}_j)^2 \\
& - \frac{2}{3} (\Delta_P^2 + \Delta_{\perp 1}^2 + \Delta_{\perp 2}^2) \},
\end{aligned} \tag{B2}$$

$$f_H = -\gamma H_\beta S_\beta + \frac{\gamma^2}{2} \chi_\perp^{-1} [(\hat{d}_\beta S_\beta)^2 \delta + S_\beta S_\beta]. \tag{B3}$$

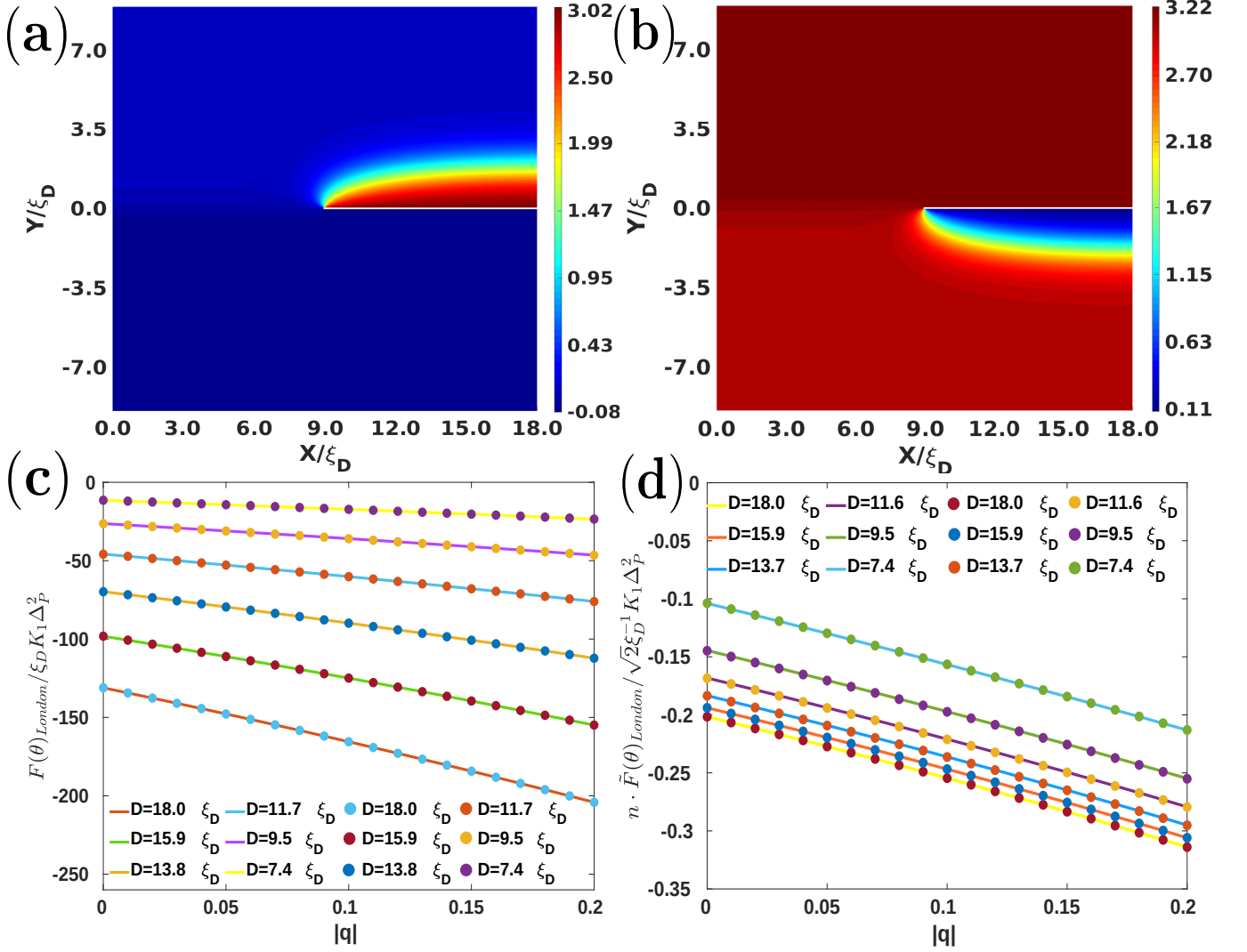


FIG. 12: Equilibrium spin textures and equilibrium London limit free energies of one-half unit cell consists of $1/4+1/4$ separable spin solitons with $\theta_{KLS} = 0$ and $\theta_{KLS} = \pi$. The dots represent data of equilibrium configurations with $\theta_{KLS} = 0$, while the solid lines represent data of equilibrium configurations with $\theta_{KLS} = \pi$. (a) is the equilibrium spin textures of one-half unit cell consists of separable spin solitons with $\theta_{KLS} = 0$, $|q| = 0.2$ and $D = 18\xi_D$. (b) is the equilibrium spin textures of one-half unit cell consists of separable spin solitons with $\theta_{KLS} = \pi$, $|q| = 0.2$ and $D = 18\xi_D$. They have same $|\Delta\theta| = \pi$ and are related by a π -rotation around \hat{x} axis. (c) depicts the equilibrium London limit free energies of spin textures with $\theta_{KLS} = 0$ and $\theta_{KLS} = \pi$ respectively. (d) depicts the surface densities of equilibrium London limit free energies of spin textures with $\theta_{KLS} = 0$ and $\theta_{KLS} = \pi$ respectively. (c) and (d) demonstrate the pseudo-random lattices consist of separable spin solitons has same equilibrium London limit free energies for boundary conditions $\theta_{KLS} = 0$ and $\theta_{KLS} = \pi$.

Then we have all of functional derivatives

$$\frac{\delta F_{hydrodynamics}}{\delta S_\beta}(\mathbf{r}') = \frac{\partial f_H}{\partial S_\beta}(\mathbf{r}') = -\gamma H_\beta + \gamma^2 \chi_\perp^{-1} [(S_\gamma \hat{d}_\gamma) \hat{d}_\beta \delta + S_\beta], \quad (\text{B4})$$

$$\begin{aligned}
\frac{\delta F_{hydrodynamics}}{\delta \hat{d}_\beta}(\mathbf{r}') &= \frac{\partial f_H}{\partial \hat{d}_\beta}(\mathbf{r}') + \frac{\partial f_{soc}}{\partial \hat{d}_\beta}(\mathbf{r}') - \partial_i \frac{f_{grad}}{\partial \partial_i \hat{d}_\beta}(\mathbf{r}') \\
&= \gamma^2 \chi_\perp^{-1} \delta S_\gamma \hat{d}_\gamma S_\beta \\
&\quad + \frac{3g_D}{5} (2\Delta_P^2 \hat{d}_\gamma \hat{z}_\gamma \hat{z}_\beta + \Delta_P \Delta_{\perp 1} \hat{z}_\beta \hat{e}_i^1 \hat{x}_i + \Delta_P \Delta_{\perp 2} \hat{z}_\beta \hat{e}_i^2 \hat{y}_i + \Delta_P \Delta_{\perp 1} \hat{z}_\beta \hat{e}_i^1 \hat{x}_i + \Delta_P \Delta_{\perp 2} \hat{z}_\beta \hat{e}_i^2 \hat{y}_i \\
&\quad + 2\Delta_P^2 \hat{d}_\gamma \hat{z}_\gamma \hat{z}_\beta + \Delta_P \Delta_{\perp 1} \hat{z}_i \hat{e}_i^1 \hat{x}_\beta + \Delta_P \Delta_{\perp 2} \hat{z}_i \hat{e}_i^2 \hat{y}_\beta + \Delta_P \Delta_{\perp 1} \hat{x}_\beta \hat{e}_i^1 \hat{z}_i + \Delta_P \Delta_{\perp 2} \hat{z}_i \hat{e}_i^2 \hat{y}_\beta) \quad (B5) \\
&\quad - \frac{1}{2} (K_1 \Delta_P^2 2\partial_i \partial_i \hat{d}_\beta + K_2 \Delta_P^2 2\partial_i \partial_j \hat{d}_\beta \hat{z}_i \hat{z}_j + 2K_2 \Delta_P \Delta_{\perp 1} \partial_i \partial_j \hat{e}_\beta^1 \hat{z}_j \hat{x}_i + 2K_2 \Delta_P \Delta_{\perp 2} \partial_i \partial_j \hat{e}_\beta^2 \hat{z}_j \hat{y}_i \\
&\quad + 2K_3 \Delta_P^2 \partial_i \partial_j \hat{d}_\beta \hat{z}_j \hat{z}_i + 2K_3 \Delta_P \Delta_{\perp 1} \hat{z}_i \partial_i \partial_j \hat{e}_\beta^1 \hat{x}_j + 2K_3 \Delta_P \Delta_{\perp 1} \partial_i \partial_j \hat{e}_\beta^2 \hat{y}_j \hat{z}_i),
\end{aligned}$$

$$\begin{aligned}
\frac{\delta F_{hydrodynamics}}{\delta \hat{e}_\beta^1}(\mathbf{r}') &= \frac{\partial f_{soc}}{\partial \hat{e}_\beta^1}(\mathbf{r}') - \partial_i \frac{f_{grad}}{\partial \partial_i \hat{e}_\beta^1}(\mathbf{r}') \\
&= \frac{3g_D}{5} (\Delta_P \Delta_{\perp 1} \hat{d}_\gamma \hat{z}_\gamma \hat{x}_\beta + \Delta_P \Delta_{\perp 1} \hat{d}_\gamma \hat{z}_\gamma \hat{x}_\beta + 2\Delta_{\perp 1}^2 \hat{e}_\gamma^1 \hat{x}_\gamma \hat{x}_\beta \\
&\quad + \Delta_{\perp 1} \Delta_{\perp 2} \hat{e}_\gamma^2 \hat{y}_\gamma \hat{x}_\beta + \Delta_P \Delta_{\perp 1} \hat{d}_\gamma \hat{x}_\gamma \hat{z}_\beta + \Delta_P \Delta_{\perp 1} \hat{d}_\gamma \hat{x}_\gamma \hat{z}_\beta) \quad (B6) \\
&\quad + \Delta_{\perp 1}^2 2\hat{e}_\gamma^1 \hat{x}_\gamma \hat{x}_\beta + \Delta_{\perp 1} \Delta_{\perp 2} \hat{e}_\gamma^2 \hat{x}_\gamma \hat{y}_\beta + \Delta_{\perp 2} \Delta_{\perp 1} \hat{e}_\gamma^2 \hat{y}_\gamma \hat{x}_\beta + \Delta_{\perp 2} \Delta_{\perp 1} \hat{e}_\gamma^2 \hat{x}_\gamma \hat{y}_\beta) \\
&\quad - \frac{1}{2} (2K_1 \Delta_{\perp 1}^2 \partial_i \partial_i \hat{e}_\beta^1 \hat{x}_j \hat{x}_j + 2K_2 \Delta_{\perp 1}^2 \partial_i \partial_j \hat{e}_\beta^1 \hat{x}_j \hat{x}_i + 2K_2 \Delta_P \Delta_{\perp 1} \partial_i \partial_j \hat{d}_\beta \hat{x}_j \hat{z}_i \\
&\quad + 2K_2 \Delta_{\perp 1} \Delta_{\perp 2} \partial_i \partial_j \hat{e}_\beta^2 \hat{x}_j \hat{y}_i \\
&\quad + 2K_3 \Delta_{\perp 1}^2 \partial_i \partial_j \hat{e}_\beta^1 \hat{x}_j \hat{x}_i + 2K_3 \Delta_P \Delta_{\perp 1} \partial_i \partial_j \hat{d}_\beta \hat{z}_j \hat{x}_i + 2K_3 \Delta_{\perp 1} \Delta_{\perp 2} \partial_i \partial_j \hat{e}_\beta^2 \hat{y}_j \hat{x}_i),
\end{aligned}$$

$$\begin{aligned}
\frac{\delta F_{hydrodynamics}}{\delta \hat{e}_\beta^2}(\mathbf{r}') &= \frac{\partial f_{soc}}{\partial \hat{e}_\beta^2}(\mathbf{r}') - \partial_i \frac{f_{grad}}{\partial \partial_i \hat{e}_\beta^2}(\mathbf{r}') \\
&= \frac{3g_D}{5} (\Delta_P \Delta_{\perp 2} \hat{d}_\gamma \hat{z}_\gamma \hat{y}_\beta + \Delta_P \Delta_{\perp 2} \hat{e}_\gamma^1 \hat{x}_\gamma \hat{y}_\gamma + \Delta_{\perp 2} \Delta_P \hat{y}_\beta \hat{d}_\gamma \hat{z}_\gamma \\
&\quad + \Delta_{\perp 2} \Delta_{\perp 1} \hat{e}_\gamma^1 \hat{x}_\gamma \hat{y}_\beta + 2\Delta_{\perp 2}^2 \hat{e}_\gamma^2 \hat{y}_\gamma \hat{y}_\beta + \Delta_P \Delta_{\perp 2} \hat{d}_\gamma \hat{y}_\gamma \hat{z}_\beta \\
&\quad + \Delta_{\perp 1} \Delta_{\perp 2} \hat{e}_\gamma^1 \hat{y}_\gamma \hat{x}_\beta + \Delta_{\perp 2} \Delta_P \hat{d}_\gamma \hat{y}_\gamma \hat{z}_\beta + \Delta_{\perp 1} \Delta_{\perp 2} \hat{e}_\gamma^1 \hat{y}_\gamma \hat{x}_\beta + \Delta_{\perp 2}^2 2\hat{e}_\gamma^2 \hat{y}_\gamma \hat{y}_\beta) \quad (B7) \\
&\quad - \frac{1}{2} (2K_1 \Delta_{\perp 2}^2 \partial_i \partial_i \hat{e}_\beta^2 \hat{y}_j \hat{y}_j + 2K_2 \Delta_{\perp 2}^2 \partial_i \partial_j \hat{e}_\beta^2 \hat{y}_j \hat{y}_i + 2K_2 \Delta_P \Delta_{\perp 2} \partial_i \partial_j \hat{d}_\beta \hat{y}_j \hat{z}_i \\
&\quad + 2K_2 \Delta_{\perp 1} \Delta_{\perp 2} \partial_i \partial_j \hat{e}_\beta^1 \hat{y}_j \hat{x}_i \\
&\quad + 2K_3 \Delta_{\perp 2}^2 \partial_i \partial_j \hat{e}_\beta^2 \hat{y}_j \hat{y}_i + 2K_3 \Delta_P \Delta_{\perp 1} \partial_i \partial_j \hat{d}_\beta \hat{z}_j \hat{y}_i \\
&\quad + 2K_3 \Delta_{\perp 1} \Delta_{\perp 2} \partial_i \partial_j \hat{e}_\beta^1 \hat{x}_j \hat{y}_i).
\end{aligned}$$

Plugging Eq. (B4), Eq. (B6), Eq. (B7) and Eq. (??) into Eq. (40) and Eq. (41), we get Eq. (43) and Eq. (44).

2. The derivation of the second order dynamic equation of spin density

Firstly we take time-derivative to Eq. (43) and get

$$\gamma \epsilon_{\alpha\beta\gamma} (H_\beta^{(0)} \frac{\partial}{\partial t} \delta S_\gamma + \frac{\partial}{\partial t} \delta H_\beta S_\gamma^{(0)}) = \epsilon_{\alpha\beta\gamma} [-\frac{6g_D}{5} Q_{\beta j}^{bd} (V_j^{d(0)} \frac{\partial}{\partial t} \delta V_\gamma^b + \frac{\partial}{\partial t} \delta V_j^d V_r^{b(0)}) + K_{ij}^{ba} (\partial_i \partial_j V_\beta^{b(0)} \frac{\partial}{\partial t} \delta V_\gamma^a + \partial_i \partial_j \frac{\partial}{\partial t} \delta V_\beta^b V_\gamma^{a(0)})], \quad (B8)$$

where

$$\begin{aligned}
\frac{\partial}{\partial t} \delta V_\alpha^a &= \{H_\beta^{(0)} V_\gamma^{a(0)} \gamma + \gamma H_\beta^{(0)} \delta V_\gamma^a + \gamma \delta H_\beta V_\gamma^{a(0)} \\
&\quad - \gamma^2 \chi_\perp^{-1} \delta (S_\eta^{(0)} V_\eta^{3(0)}) (V_\beta^{3(0)} \delta V_\gamma^a + V_\gamma^{3(0)} \delta V_\beta^3) + \gamma^2 \chi_\perp^{-1} (S_\beta^{(0)} V_\gamma^{a(0)} + S_\beta^{(0)} \delta V_\gamma^a + \delta S_\beta V_\gamma^{a(0)})\} \epsilon_{\alpha\beta\gamma}. \quad (B9)
\end{aligned}$$

Taking into account the relations:

$$\gamma S_\beta^{(0)} = H_\alpha^{(0)} \chi_{\alpha\beta}, \quad V_\eta^{3(0)} S_\eta^{(0)} = \hat{\mathbf{d}}^{(0)} \cdot \mathbf{S}^{(0)} = 0, \quad (B10)$$

where magnetic susceptibility $\chi_{\alpha\beta} = \chi_{\parallel}\delta_{\alpha\beta} - (\chi_{\perp} - \chi_{\perp})\hat{d}_{\alpha}^{(0)}\hat{d}_{\beta}^{(0)}$, Eq. (B9) is simplified to

$$\frac{\partial}{\partial t}\delta V_{\alpha}^a = \epsilon_{\alpha\beta\gamma}V_{\gamma}^{a(0)}(\gamma\delta H_{\beta}^{a(0)} - \gamma^2\chi_{\perp}^{-1}\delta S_{\beta}) \quad (\text{B11})$$

Taking Eq. (B11) back into Eq. (B8), we get

$$\frac{\partial^2}{\partial t^2}\delta S_{\alpha} = \gamma\epsilon_{\alpha\beta\gamma}(H_{\beta}^{(0)}\frac{\partial}{\partial t}\delta S_{\gamma} + \frac{\partial}{\partial t}\delta H_{\beta}S_{\gamma}^{(0)}) + \Xi_{\alpha\lambda}\delta S_{\lambda} + C_{\alpha\eta}\delta H_{\eta} \quad (\text{B12})$$

3. The derivation of transverse NMR response equation

In the limit of $|\omega - \omega_L| \ll \omega_L$ and under parametrization Eq. (10), Eq. (47) are

$$\begin{aligned} i\omega\delta S_2(\omega) &= -\gamma S_3^{(0)}\delta H_1(\omega), \\ i\omega\delta S_1(\omega) &= \gamma H_2^{(0)}\delta S_3(\omega) + \frac{\Xi_{11}}{i\omega}\delta S_1(\omega) + \frac{\Xi_{13}}{i\omega}\delta S_3(\omega) + \frac{C_{31}}{i\omega}\delta H_1(\omega), \\ i\omega\delta S_3(\omega) &= \gamma[S_2^{(0)}\delta H_1(\omega) - H_2^{(0)}\delta S_1(\omega)] + \frac{\Xi_{31}}{i\omega}\delta S_1(\omega) + \frac{\Xi_{33}}{i\omega}\delta S_3(\omega) + \frac{C_{31}}{i\omega}\delta H_1(\omega). \end{aligned} \quad (\text{B13})$$

We expand ω around ω_L as $\omega = \omega_L + \epsilon + O^2(\epsilon)$, then we get

$$\delta S_1(\omega) = \frac{\delta S_3(\omega)}{i(1+\epsilon)}, \quad \delta S_3(\omega) = \frac{1}{i(1+\epsilon)}\left(\frac{\chi_{\perp}}{\gamma}\delta H_1(\omega) - \delta S_1(\omega)\right), \quad (\text{B14})$$

where $\epsilon = (\omega - \omega_L)$. By multiplying $i\omega$ and utilizing Eq. (B14), Eq. (??) can be reorganized as

$$\begin{aligned} (\omega^2 - \omega_L^2)(\delta S_1(\omega) + i\delta S_3(\omega)) &= i[-\Xi_{31}\left(\frac{\delta S_1}{1+2\epsilon} + i\frac{\delta S_3}{1+2\epsilon}\right) + \Xi_{13}\left(\frac{\delta S_1}{1+2\epsilon} + i\delta S_3\right)] \\ &\quad + \frac{\Xi_{11}}{1+\epsilon}(\delta S_1 + i\delta S_3) + \frac{\Xi_{33}}{1+\epsilon}(\delta S_1 + i\delta S_3) \end{aligned} \quad (\text{B15})$$

$$- (C_{11} + iC_{31})\delta H_1 - \frac{\chi_{\perp}}{\gamma}\left(\frac{\Xi_{33}}{1+\epsilon} + i\frac{\Xi_{13}}{1+2\epsilon} - i\frac{\Xi_{31}}{1+2\epsilon}\right)\delta H_1. \quad (\text{B16})$$

In the case of $\epsilon \rightarrow 0$, this gives Eq. (50).

4. All $\Xi_{\alpha\lambda}$ terms in Eq. (52)

By utilizing Eq. (48) and parametrization Eq. (10), we have

$$\begin{aligned} \Xi_{11} + \Xi_{33} &= [2c_1(K_1 + K_2 + K_3)\Delta_{\perp 2}^2 + c_1K_1(\Delta_{\perp 1}^2 + \Delta_P^2)]\partial_y\partial_y\delta S_+ \\ &\quad + [c_1(K_1 + K_2 + K_3)\Delta_{\perp 1}^2 + c_1K_1(2\Delta_{\perp 2}^2 + \Delta_P^2)]\partial_x\partial_x\delta S_+ \\ &\quad + c_2(\Delta_P + \Delta_{\perp 1})[-(\Delta_{\perp 1} + \Delta_P)\cos 2\theta - 5\Delta_{\perp 2}\sin\theta] + c_2(\Delta_P^2 + \Delta_{\perp 1}^2 + 4\Delta_{\perp 2}^2), \end{aligned} \quad (\text{B17})$$

$$\begin{aligned} \Xi_{13} + \Xi_{31} &= -2c_1K_1\Delta_P^2\partial_i\delta S_+\partial_i\theta - 2c_1\Delta_{\perp 1}^2[K_1\partial_y\delta S_+\partial_y\theta + (K_1 + K_2 + K_3)\partial_x\delta S_+\partial_x\theta\cos 2\theta] \\ &\quad - c_1\{[K_1\Delta_P^2 + (K_1 + K_2 + K_3)\Delta_{\perp 1}^2]\partial_x\partial_x\theta + K_1(\Delta_P^2 + \Delta_{\perp 1}^2)\partial_y\partial_y\theta\}, \end{aligned} \quad (\text{B18})$$

where

$$c_1 = \frac{\gamma^2}{\chi_{\perp}}, \quad c_2 = \frac{6g_D\gamma^2}{5\chi_{\perp}}. \quad (\text{B19})$$

plugging Eq. (B18), Eq. (B19) into Eq. (52) and multiplying $\tilde{\Omega}^{-2}$ on both sides, we get

$$\begin{aligned} \frac{\omega^2 - \omega_L^2}{\tilde{\Omega}^2} \delta S_+ = & \left\{ \frac{5}{6g_D} [6K_1\rho_2^2 + K_1(\rho_1^2 + 1)] \partial_y \partial_y + \frac{5}{6g_D} [3K_1\rho_1^2 + K_1(2\rho_2^2 + 1)] \partial_x \partial_x \right. \\ & \left. - i \frac{10}{6g_D} [(K_1 + 3\rho_1^2 K_1 \cos 2\theta) \partial_x \theta \partial_x - K_1(1 + \rho_1^2) \partial_y \theta \partial_y] \right\} \delta S_+ \end{aligned} \quad (\text{B20})$$

$$\begin{aligned} & - i \frac{5}{6g_D} [K_1(1 + 3\rho_1^2) \partial_x \partial_x \theta + K_1(1 + \rho_1^2) \partial_y \partial_y \theta] \delta S_+ \\ & + \{(1 + \rho_1)[-(1 + \rho_1) \cos 2\theta - 5\rho_2 \sin \theta] + (1 + \rho_1^2 + 4\rho_2^2)\} \delta S_+. \end{aligned} \quad (\text{B21})$$

To simplify Eq. (B25), we need the Lagrangian equation of θ

$$\begin{aligned} \frac{\delta F_{London}(\theta)}{\delta \theta} = & c_1 \{ [K_1 \Delta_P^2 + (K_1 + K_2 + K_3) \Delta_{\perp 1}^2] \partial_x \partial_x \theta + K_1 (\Delta_P^2 + \Delta_{\perp 1}^2) \partial_y \partial_y \theta \} \\ & - c_2 \{ \Delta_{\perp 2} (\Delta_P + \Delta_{\perp 1}) \cos \theta + (\Delta_P + \Delta_{\perp 1})^2 \sin 2\theta \} = 0. \end{aligned} \quad (\text{B22})$$

This equation can be simplified to

$$(1 + 3\rho_1^2) \partial_x \partial_x \theta + (1 + \rho_1^2) \partial_y \partial_y \theta = (1 + \rho_1)^2 \sin 2\theta - (1 + \rho_1) \rho_2 \cos \theta. \quad (\text{B23})$$

Then Eq. (B25) can be written as

$$\begin{aligned} \frac{\omega^2 - \omega_L^2}{\tilde{\Omega}^2} \delta S_+ = & \left\{ \frac{5}{6g_D} [6K_1\rho_2^2 + K_1(\rho_1^2 + 1)] \partial_y \partial_y + \frac{5}{6g_D} [3K_1\rho_1^2 + K_1(2\rho_2^2 + 1)] \partial_x \partial_x \right. \\ & \left. - i \frac{10}{6g_D} [(K_1 + 3\rho_1^2 K_1 \cos 2\theta) \partial_x \theta \partial_x - K_1(1 + \rho_1^2) \partial_y \theta \partial_y] \right\} \delta S_+ \end{aligned} \quad (\text{B24})$$

$$\begin{aligned} & - i \frac{5K_1}{6g_D} \xi_D^{-2} [(1 + \rho_1)^2 \sin 2\theta - (1 + \rho_1) \rho_2 \cos \theta] \delta S_+ \\ & + \{(1 + \rho_1)[-(1 + \rho_1) \cos 2\theta - 5\rho_2 \sin \theta] + (1 + \rho_1^2 + 4\rho_2^2)\} \delta S_+. \end{aligned} \quad (\text{B25})$$

This is Eq. (53).

Appendix C: Spin dynamic response Of soliton ($|\Delta\theta| = \pi - 2\theta_0$) and big Soliton ($|\Delta\theta| = \pi + 2\theta_0$)

-
- * Electronic address: kuang.zhang@aalto.fi
- ¹ T. W. B. Kibble, G. Lazarides and Q. Shafi, Walls Bounded by Strings, Phys. Rev. D 26, 435 (1982).
 - ² T. W. B. Kibble, Classification of Topological Defects and Their Relevance to Cosmology and Elsewhere, In: Bunkov Y.M., Godfrin H. (eds) Topological Defects and the Non-Equilibrium Dynamics of Symmetry Breaking Phase Transitions, NATO Science Series (Series C: Mathematical and Physical Sciences), vol. 549, pp. 7–31, Springer, Dordrecht (2000).
 - ³ A. Vilenkin and A. E. Everett, Cosmic Strings and Domain Walls in Models with Goldstone and PseudoGoldstone Bosons, Phys. Rev. Lett. 48, 1867 (1982).
 - ⁴ A. E. Everett and A. Vilenkin, Left-right Symmetric Theories and Vacuum Domain Walls and Strings, Nucl. Phys. B 207, 43 (1982).
 - ⁵ Y. B. Zeldovich, I. Y. Kobzarev and L. B. Okun, Cosmological Consequences of the Spontaneous Breakdown of Discrete Symmetry, Zh. Eksp. Teor. Fiz. 67, 3 (1974) [Sov. Phys. JETP 40, 1 (1974)].
 - ⁶ G. Lazarides and Q. Shafi, Axion Models with No Domain Wall Problem, Phys. Lett. 115 B (1982) 2125.
 - ⁷ R. Sato, F. Takahashi and M. Yamada, Unified Origin of Axion and Monopole Dark Matter, and Solution to the Domain-wall Problem, Phys. Rev. D 98, no. 4, 043535 (2018).
 - ⁸ C. Chatterjee, T. Higaki, and M. Nitta, Note on a solution to domain wall problem with the Lazarides-Shafi mechanism in axion dark matter models, Phys. Rev. D 101, 075026 (2020).
 - ⁹ A. Caputo, M. Reig, Cosmic implications of a low-scale solution to the axion domain wall problem, Phys. Rev. D 100, 063530 (2019).
 - ¹⁰ Xi Chen, Eva Korblova, Dengpan Dong, Xiaoyu Wei, Renfan Shao, Leo Radzihovsky, Matthew A. Glaser, Joseph E. Maclennan, Dmitry Bedrov, David M. Walba, and Noel A. Clark, First-principles experimental demonstration of ferroelectricity in a thermotropic nematic liquid crystal: Polar domains and striking electro-optics, Proc. Natl. Acad. Sci. U.S.A., 10.1073/pnas.2002290117 (2020).

- ¹¹ Oleg D. Lavrentovich, Ferroelectric nematic liquid crystal, a century in waiting, PNAS. **117** (26) 14629-14631 (2020).
- ¹² V. V. Dmitriev, A. A. Senin, A. A. Soldatov, E. V. Surovtsev, and A. N. Yudin, B phase with polar distortion in superfluid ^3He in ordered aerogel. JETP. **119**, 10881096 (2014).
- ¹³ S. Yang, R. Ikeda, Possibility of unconventional pairing states in superfluid ^3He in uniaxially anisotropic aerogels, J. Phys. Soc. Jpn **83**, 084602 (2014).
- ¹⁴ M. Tange, R. Ikeda, Half-quantum vortex pair in polar-distorted B phase of superfluid ^3He in aerogels, Phys. Rev. B. **101**, 094512 (2020).
- ¹⁵ A.B. Vorontsov and J. A. Sauls, Crystalline order in superfluid ^3He films, Phys. Rev. Lett. **98**, 045301 (2007).
- ¹⁶ L.V. Levitin, B. Yager, L. Sumner, B. Cowan, A.J. Casey, J. Saunders, N. Zhelev, R.G. Bennett, and J.M. Parpia, Evidence for a spatially modulated superfluid phase of ^3He under confinement, Phys. Rev. Lett. **122**, 085301 (2019).
- ¹⁷ J. Shook, V. Vadakumbatt, P. Senarath Yapa, C. Doolin, R. Boyack, P.H. Kim, G.G. Popowich, F. Souris, H. Christani, J. Maciejko, J.P. Davis, Stabilized pair density wave via nanoscale confinement of superfluid ^3He -A, Phys. Rev. Lett. **124**, 015301 (2020).
- ¹⁸ R.Sh. Askhadullin, V.V. Dmitriev, D.A. Krasnikhin, P.N. Martynov, A.A. Osipov, A.A. Senin, A.N. Yudin, Phase diagram of superfluid ^3He in "nematically ordered" aerogel, JETP. Lett. **95**, 326 (2012).
- ¹⁹ P. W. Anderson, Theory of dirty superconductors, J. Phys. Chem. Solids **11**, 26–30 (1959).
- ²⁰ I.A. Fomin, Analog of Anderson theorem for the polar phase of liquid ^3He in nematic aerogel, JETP **127**, 933–938 (2018).
- ²¹ I.A. Fomin, Temperature dependence of the order parameter of the polar phase of liquid ^3He in nematic aerogel, arXiv:2003.09652.
- ²² V.B. Eltsov, T. Kamppinen, J. Rysti, and G.E. Volovik, Topological nodal line in superfluid ^3He and the Anderson theorem, arXiv:1908.01645 (2019).
- ²³ A. Ramires, D. F. Agterberg and M. Sigrist, Tailoring T_c by symmetry principles: The concept of superconducting fitness, Phys. Rev. B **98**, 024501 (2018).
- ²⁴ A. S. Schwarz, Field Theories With No Local Conservation Of The Electric Charge, Nucl. Phys. B **208**, 141 (1982).
- ²⁵ J. E. Kiskis, Disconnected Gauge Groups and the Global Violation of Charge Conservation, Phys. Rev. D **17**, 3196 (1978).
- ²⁶ G.E. Volovik and V.P. Mineev, Line and point singularities in superfluid ^3He , JETP Lett. **24**, 561–563 (1976).
- ²⁷ M.C. Cross and W.F. Brinkman, Textural singularities in superfluid A-phase of ^3He , J. Low Temp. Phys. **27**, 683–686 (1977).
- ²⁸ M.M. Salomaa, G.E. Volovik, Half-quantum vortices in superfluid ^3He -A, Phys. Rev. Lett. **55**, 1184–1187 (1985).
- ²⁹ Chia-Ren Hu and K. Maki, Satellite magnetic resonances of a bound pair of half-quantum vortices in rotating superfluid ^3He -A, Phys. Rev. B **36**, 6871–6880 (1987).
- ³⁰ V. Vakaryuk and A.J. Leggett, Spin polarization of half-quantum vortex in systems with equal spin pairing, Phys. Rev. Lett. **103**, 057003 (2009).
- ³¹ G.E. Volovik, Fermion zero modes on vortices in chiral superconductors, JETP. Lett. **70**, 609–614 (1999); cond-mat/9909426.
- ³² N. Read and D. Green, Paired states of fermions in two dimensions with breaking of parity and time-reversal symmetries and the fractional quantum Hall effect, Phys. Rev. B **61**, 10267–10297 (2000).
- ³³ D.A. Ivanov, Non-abelian statistics of half-quantum vortices in p-wave superconductors, Phys. Rev. Lett. **86**, 268 (2001).
- ³⁴ S. Autti, V. V. Dmitriev, J. T. Mkinen, A. A. Soldatov, G. E. Volovik, A. N. Yudin, V. V. Zavjalov, and V. B. Eltsov, Observation of Half-Quantum Vortices in Topological Superfluid ^3He , Phys. Rev. Lett. **117**, 255301 (2016).
- ³⁵ J.T. Mäkinen, V.V. Dmitriev, J. Nissinen, J. Rysti, G.E. Volovik, A.N. Yudin, K. Zhang, V.B. Eltsov, Half-quantum vortices and walls bounded by strings in the polar-distorted phases of topological superfluid ^3He , Nat. Comm. **10**, 237 (2019).
- ³⁶ D. Vollhardt and P. Wölfle, *The superfluid phases of helium 3* (Taylor and Francis, London, 1990).
- ³⁷ G. E. Volovik and K. Zhang, String monopoles, string walls, vortex-skyrmions and nexus objects in polar distorted B-phase of ^3He , Phys. Rev. Research **2**, 023263 (2020).
- ³⁸ Charles Nash, Siddhartha Sen, *Topology and Geometry for Physicists* (Academic Press, 1988).
- ³⁹ E. V. Thuneberg, Identification of vortices in superfluid ^3He -B, Phys. Rev. Lett. **56**, 359–362 (1986).
- ⁴⁰ G.E. Volovik and M.M. Salomaa, Spontaneous breaking of axial symmetry in v -vortices in superfluid ^3He -B, JETP. Lett. **42**, 521–524 (1985).
- ⁴¹ Y. Kondo, J.S. Korhonen, M. Krusius, V.V. Dmitriev, Yu. M. Mukharskiy, E.B. Sonin and G.E. Volovik, Direct observation of the nonaxisymmetric vortex in superfluid ^3He -B, Phys. Rev. Lett. **67**, 81–84 (1991).
- ⁴² G. E. Volovik, Half quantum vortices in the B phase of superfluid ^3He , JETP. Lett. **52**, 358 (1990).
- ⁴³ M.A. Silaev, E.V. Thuneberg, and M. Fogelström, Lifshitz Transition in the Double-Core Vortex in ^3He -B, Phys. Rev. Lett. **115**, 235301 (2015).
- ⁴⁴ G. E. Volovik, On Larkin-Imry-Ma State of ^3He -A in Aerogel. J Low Temp Phys **150**, 453463 (2008).
- ⁴⁵ V. P. Mineyev and G. E. Volovik, Planar and linera solitiosn in superfluid ^3He , Phys. Rev. B **18**, 3197 (1978).
- ⁴⁶ Seji Kang, Sang Won Seo, Hiromitsu Takeuchi, and Y. Shin, Observation of Wall-Vortex Composite Defects in a Spinor Bose-Einstein Condensate, Phys. Rev. Lett. **122**, 095301 (2019).
- ⁴⁷ I-Kang Liu, Shih-Chuan Gou, H. Takeuchi, Phase diagram of solitons in the polar phase of a Spin-1 Bose-Einstein condensate, arXiv: 2002.06088.
- ⁴⁸ Masaki Tange and Ryusuke Ikeda, Half-quantum vortex pair in the polar-distorted B phase of superfluid ^3He in aerogels, Phys. Rev. B **101**, 094512 (2020).
- ⁴⁹ G. E. Volovik, *Exotic Properties of Superfluid Helium 3* (World Scientific, 1992).
- ⁵⁰ Jorge Nocedal, Stephen. J. Wright, *Numerical Optimization* (Springer, New York, 2006)
- ⁵¹ G. E. Volovik, J. Rysti, J. T. Makinen, V. B. Eltsov, Spin, orbital, Weyl and other glasses in topological superfluids, J. Low. Temp. Phys. **196**, 82 (2019).

- ⁵² A. Altland and Ben. D. Simons *Condensed Matter Field Theory* (Cambridge University Press, 2 edition 2010).
- ⁵³ P. W. Anderson, Some Macroscopic Considerations on Motions of Anisotropic Superfluids, *Phys. Rev. Lett.* **30**, 368 (1973).
- ⁵⁴ P. W. Anderson, C. Varma, Properties of a Possible Superfluid State of ^3He . *Nature* **241**, 187 (1973).
- ⁵⁵ P. M. Chaikin, T. C. Lubensky, *Principles of Condensed Matter Physics*, (Cambridge University Press, 1995).
- ⁵⁶ I.E.Dzyaloshinskii and G.E. Volovick, Poisson brackets in condensed matter physics, *Annals of Physics*, **125**, 67-97 (1980)
- ⁵⁷ P. G. Ciarlet, *The Finite Element Method for Elliptic Problems*, (North Holland, 1978).
- ⁵⁸ Y. Kondo, J.S. Korhonen, M. Krusius, V.V. Dmitriev, E.V. Thuneberg and G.E. Volovik, Combined spin - mass vortices with soliton tail in superfluid $^3\text{He-B}$, *Phys. Rev. Lett.* **68**, 3331 (1992).
- ⁵⁹ P. W. Anderson and G. Toulouse, Phase slippage without vortex cores: vortex textures in superfluid ^3He , *Phys. Rev. Lett.* **38**, 508–511 (1977).
- ⁶⁰ V.R. Chechetkin, Types of vortex solutions in superfluid ^3He , *JETP* **44**, 766–772 (1976).
- ⁶¹ G.E. Volovik, N.B. Kopnin, On the rotating ^3He - A, *Pis'ma. Zh. Eksp. Teor. Fiz.* **25**, 26–28 (1977); *JETP Lett.* **25**, 22–24 (1977).
- ⁶² H.K. Sepl, P.J. Hakonen, M. Krusius, T. Ohmi, M.M. Salomaa, J.T. Simola, and G.E. Volovik, Continuous vortices with broken symmetry in rotating superfluid $^3\text{He-A}$, *Phys. Rev. Lett.* **52**, 1802–1805 (1984).
- ⁶³ J.P. Pekola, K. Torizuka, A.J. Manninen, J.M. Kyynrinen and G.E. Volovik, Observation of a topological transition in the $^3\text{He-A}$ vortices, *Phys. Rev. Lett* **65**, 32933296 (1990).
- ⁶⁴ T. W. B. Kibble and T. Vachaspati, Monopoles on strings, *J. Phys. G* **42**, 094002 (2015).
- ⁶⁵ A. Saurabh and T. Vachaspati, Monopoleantimonopole: interaction, scattering and creation, *Phil. Trans. R. Soc. A* **377**, 20190143 (2019).
- ⁶⁶ G. Lazarides and Q. Shafi, Monopoles, Strings, and Necklaces in $\text{SO}(10)$ and E_6 , *J. High Energ. Phys.* **2019**, 193 (2019).
- ⁶⁷ G.E. Volovik, Composite topological objects in topological superfluids, arXiv:1912.05962.